Optical spectroscopy study of two-dimensional materials

12

Miao-Ling Lin[a] *and Ping-Heng Tan*[a,b]
[a]State Key Laboratory of Superlattices and Microstructures, Institute of Semiconductors, Chinese Academy of Sciences, Beijing, China, [b]Center of Materials Science and Optoelectronics Engineering and CAS Center of Excellence in Topological Quantum Computation, University of Chinese Academy of Sciences, Beijing, China

12.1 Two-dimensional systems

Two-dimensional materials (2DMs) are easily exfoliable from their three-dimensional (3D) parent crystals due to the strong in-plane covalent bonds and weak interlayer van der Waals (vdW) interactions [1]. Because the physical properties in few-layer 2DMs change significantly in comparison with their bulk counterparts [2, 3], they have served as promising candidates for the applications in next-generation nanoelectronics and optoelectronics since the first discovery of a truly 2DM of graphene [4]. The two-dimensional (2D) databases consist of the graphene family (e.g., graphene [4, 5], hexagonal boron nitride [hBN] [6]), 2D dichalcogenides (e.g., MX_2, M=Mo, W, X=S, Se, Te [7]), 2D oxides (e.g., MoO_3, WO_3 [8]) and perovskite families (e.g., halide perovskite [9]), ranging from metals (e.g., $NbSe_2$ [10], TaS_2 [11]), semimetals (e.g., graphene, WTe_2 [12]), semiconductors (e.g., MoS_2 [13]) to insulators (e.g., hBN). In fact, Mounet et al. identified 5619 layered compounds from 108,423 experimentally known 3D compounds by high-throughput calculations, in which 1036 compounds are easily exfoliable and 789 compounds are potentially exfoliable [1]. According to the space group and structure similarities, the 1036 easily exfoliable compounds can be divided into 562 prototypes, among which the 10 most common ones, representing a total of 214 structures, are shown in Fig. 12.1A. Except for the FeOCl-like prototype, all these common prototypes have high-order rotational axes, especially the threefold rotational axes. The MX_2-like prototype is the most common with 64 similar structures included [14], to which many transition metal dichalcogenides (TMDs) and dihalides belong. Until now, the prototypes of CdI_2 (e.g., SnS_2 [15], etc.), MoS_2, and $FePS_3$ [16, 17] are compelling and attract much attention, while the $NdTe_3$ prototype common to many rare-earth tritellurides has not been reported.

The 2DMs with different number of layers may belong to different space groups due to the varied out-of-plane translational symmetry. Furthermore, because of the interlayer coupling, the number of layers provides a new degree of freedom for manipulating novel properties of 2DMs. For example, the semiconductor MX_2 undergoes a transition from indirect-gap semiconductor of bulk material to direct-gap

Modeling, Characterization and Production of Nanomaterials. https://doi.org/10.1016/B978-0-12-819905-3.00012-9

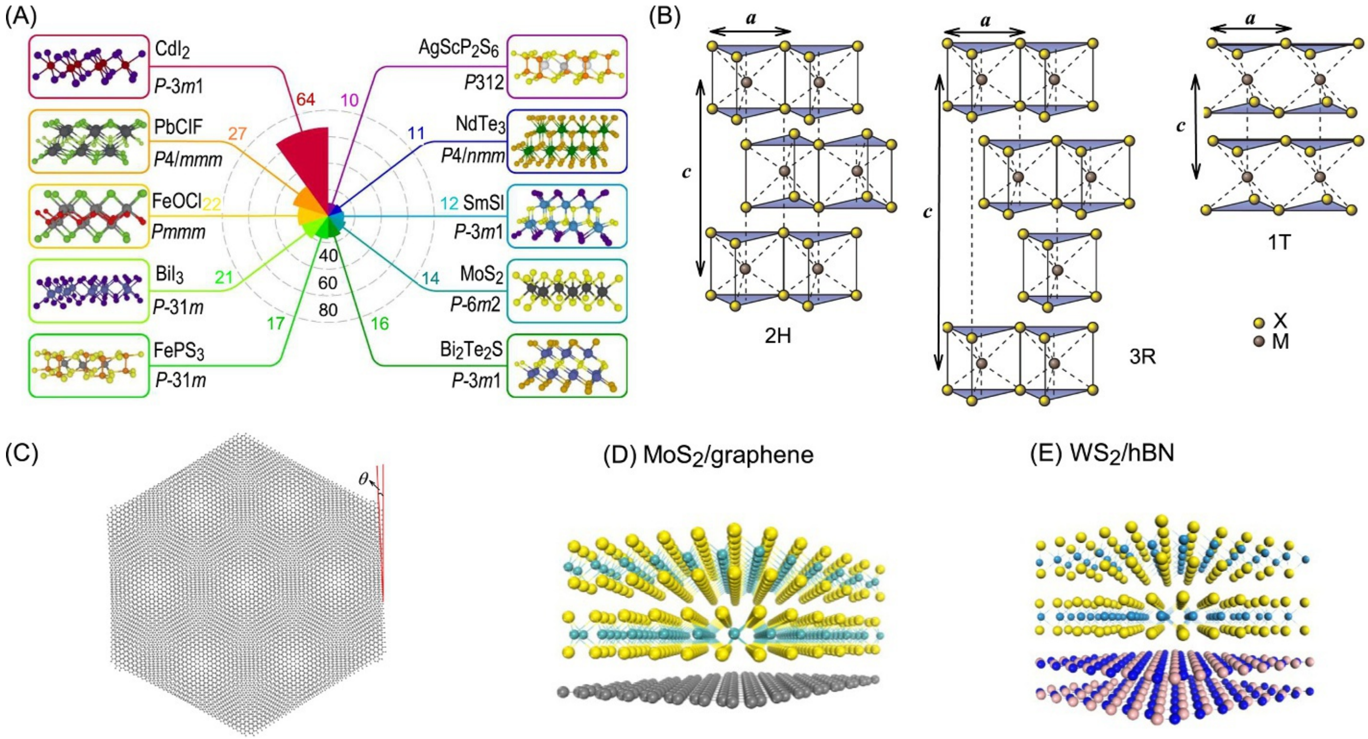

Fig. 12.1 (A) The most common 2D structural prototypes, together with the structure-type formula and the space group of the 2D systems. (B) Schematic diagrams of the three typical structural polytypes of MX_2 (M=Mo, W, X=S, Se, Te): 2H, 3R, and 1T. *a* and *c* represent the in-plane and out-of-plane lattice constants, respectively. (C) A typical schematic for twisted bilayer graphene with the twist angle of θ. The schematics of two vdWHs: (D) MoS_2/graphene and (E) WS_2/hBN.

(A) Adapted from N. Mounet, M. Gibertini, P. Schwaller, D. Campi, A. Merkys, A. Marrazzo, T. Sohier, I.E. Castelli, A. Cepellotti, G. Pizzi, N. Marzari, Two-dimensional gas of massless Dirac fermions in graphene, Nat. Nanotechnol. 13 (3) (2018) 246–252, https://doi.org/10.1038/s41565-017-0035-5; (B) adapted from Q.H. Wang, K. Kalantar-Zadeh, A. Kis, J.N. Coleman, M.S. Strano, Electronics and optoelectronics of two-dimensional transition metal dichalcogenides, Nat. Nanotechnol. 7 (11) (2012) 699–712, https://doi.org/10.1038/nnano.2012.193.

semiconductor of the monolayer [13]. In addition, for a 2DM with a given number of layers N (NL-2DM), the stacking order of the repeated rigid layer in the c-axis can be different, leading to various structural polytypes [14, 18], as one typical example of MX_2 depicted in Fig. 12.1B. There are two common polytypes, 2H (H: hexagonal) and 3R (R: rhombohedral) for the stacking of 1H-MX_2, in which the ith layer in 2H stacking is rotated by 180 degrees with respective to the $(i-1)$th layer while the adjacent layer undergoes a shift in 3R stacking. Thus, inversion symmetry exists in the even N layered (ENL) 2H-MX_2 but not in the odd N layered (ONL) 2H-MX_2. Furthermore, the metal atoms can also behave in octahedral coordination to generate the 1T stacking. The 2H-, 3R-, and 1T-stacked trilayer MX_2 belong to D_{3h}, C_{3v}, and D_{3d} symmetries, respectively, resulting in distinct novel electronic and optical properties [18, 19]. As the 2H stacking is the most common and stable stacking for MX_2, we only refer to 2H-stacked MX_2 when we talk about MX_2 later without any emphasis. In addition to the natural stacking orders for 2DMs, the twisted stacking can be naturally generated in a mechanical exfoliation process or formed by wet/dry transfer [20, 21]. Fig. 12.1C plots one typical schematic of the twisted bilayer graphene (tBLG) with a twist angle of θ, in which the moiré patterns are obviously observed. Twisted stacking can also occur between the constituents with different number of layers, forming the twisted multilayer 2DM (also denoted as $t(m+n+\cdots)$ L-2DM, $N=m+n+\cdots$). Besides, the van der Waals heterostructures (vdWHs) have recently emerged as an additional avenue to engineer new physical properties by assembling various 2DMs together in a desired fashion, since they exhibit remarkable electronic and optical properties compared with their constituents [22]. Fig. 12.1D and E shows the schematic diagrams of MoS_2/graphene and WS_2/hBN heterostructures, respectively. In twisted systems or the vdWHs formed by constituents with nearly the same lattice constants, the moiré superlattice can be generated at the interface, which can periodically modulate the behaviors of electrons [23], excitons [24], and phonons [25]. The features of moiré bands can be revealed by the transport properties [26], while the so-called moiré excitons and phonons have been probed via photoluminescence [27–29] and Raman spectroscopy [25], respectively.

The sensitivity of electronic and optical properties of 2DMs to the number of layers, stacking order, and assemblies in their hybrid systems have captured the interest of the scientific community to expand the understanding in fundamental physics behind the 2DMs and related vdWHs. Optical spectroscopy techniques, including optical contrast (OC), photoluminescence (PL) spectroscopy, Rayleigh scattering, Raman spectroscopy, and second-harmonic generation (SHG), serve as powerful techniques to investigate the electronic and optical properties through light-matter interactions. This chapter is organized as follows: Section 12.2 addresses the OC and differential reflection spectrum in 2DMs as useful tools for thickness and exciton level characterization. The typical PL spectra in semiconductor MX_2 and their valley polarization are demonstrated in detail in Section 12.3. The signatures of the moiré excitons of vdWHs in PL are also included. A simple introduction to Rayleigh scattering is given in Section 12.4. Section 12.5 provides a broad review of the Raman spectroscopy in pristine 2DMs, twisted 2DMs, and vdWHs. And finally, Section 12.6 presents the recent works on SHG in 2DMs.

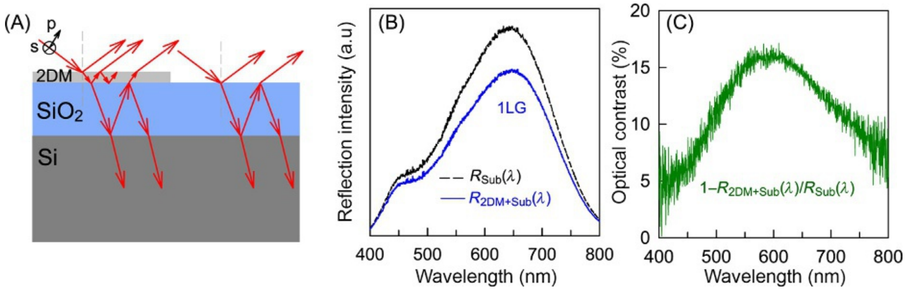

Fig. 12.2 (A) Schematic diagrams of multiple reflection and optical interference in the multilayered structures containing air, 2DM, SiO_2, and Si for the incident and outgoing light. *s* and *p* represent the *s*- and *p*-polarization components of the incident light, respectively. (B) The reflection spectra from bare SiO_2/Si substrate (R_{sub}) and from 1LG on the substrate ($R_{\mathrm{2DM+sub}}$). (C) The corresponding OC for 1LG.

12.2 Optical contrast

By depositing a thin film onto a substrate with multilayer structure, varied multiple reflection and optical interference occur in thin films on substrate and the bare substrate, resulting in significantly different reflected light intensity of thin film from the bare substrate [30, 31], as shown in Fig. 12.2A. The relative intensity of reflection light between the thin film on substrate and the bare substrate is defined as the OC of the thin film. For physical characterization and device applications, 2DMs are usually deposited onto the SiO_2/Si or quartz substrates, which leads to a multilayer structure consisting of air, 2DMs, and substrates. The OC of 2DMs on substrate can be calculated by [31]

$$\mathrm{OC}(\lambda) = 1 - R_{\mathrm{2DM+sub}}(\lambda)/R_{\mathrm{sub}}(\lambda), \tag{12.1}$$

where $R_{\mathrm{2DM+sub}}$ (λ) and R_{sub} (λ) are the reflection light intensity from 2DMs on substrate and that of bare substrate, respectively. Due to the multiple reflection interference and the wavelength-dependent complex refractive index of 2DMs and substrates, the reflection light intensity and thus the OC are dependent on the wavelength (λ) of the incident light, as an example of monolayer graphene (1LG) on 90 nm SiO_2/Si substrate shown in Fig. 12.2B and C. The setup for OC (λ) under backscattering configuration is demonstrated in detail in [31]. The OC (λ) of 2DMs on a substrate makes them be visible by the naked eye through a microscope, which can be further utilized to identify the number of layers, as discussed later.

From the perspective of theoretical calculation, OC (λ) can be quantitatively calculated by the transfer matrix based on the multiple reflection interference method [32, 33], in which the electric and magnetic components in each medium are connected by the multiplication of characteristic matrices. The detailed calculation has been reported [32]. The calculated OC (λ) is determined by the wavelength (λ),

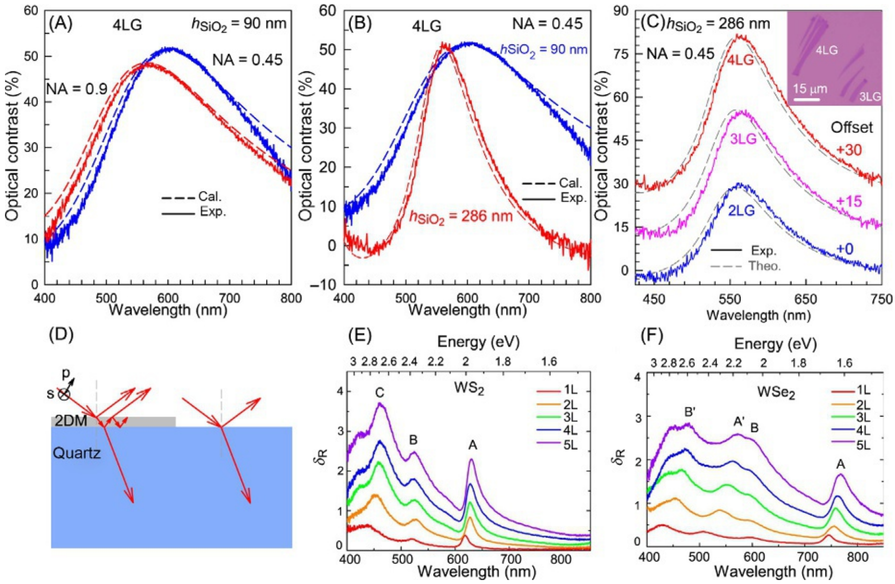

Fig. 12.3 (A) The theoretical and experimental OC (λ) of 4LG on a SiO$_2$/Si substrate (h_{SiO2} = 90 nm) with objectives of NA = 0.45 and NA = 0.9. (B) The theoretical and experimental OC (λ) of 4LG on SiO$_2$/Si substrates of h_{SiO2} = 90 nm and h_{SiO2} = 286 nm using an objective with NA = 0.45. (C) The theoretical and experimental OC (λ) of 2LG, 3LG, and 4LG on SiO$_2$/Si substrate of h_{SiO2} = 286 nm with an objective of NA = 0.45; the *inset* represents the optical images of 3LG and 4LG. (D) Schematic diagrams for the incident and outgoing light in the multilayer containing air, 2DM, and quartz. *s* and *p* represent the *s*- and *p*-polarization components of the incident light, respectively. Differential reflectance spectra of mechanically exfoliated (E) 2H-WS$_2$ and (F) 2H-WSe$_2$ with one to five layers. The peaks are labeled. (C) Adapted from Y. Lu, X.-L. Li, X. Zhang, J.-B. Wu, P.-H. Tan, Optical contrast determination of the thickness of SiO$_2$ film on Si substrate partially covered by two-dimensional crystal flakes, Sci. Bull. 60 (8) (2015) 806–811, https://doi.org/10.1007/s11434-015-0774-3; (E, F) adapted from W. Zhao, Z. Ghorannevis, L. Chu, M. Toh, C. Kloc, P.-H. Tan, G. Eda, Evolution of electronic structure in atomically thin sheets of WS$_2$ and WSe$_2$, ACS Nano 7 (1) (2013) 791–797, https://doi.org/10.1021/nn305275h.

numerical aperture (NA) of the objective, complex refractive index, and thickness of each dielectric medium. Fig. 12.3A shows the theoretical and experimental OC (λ) of one four-layer graphene (4LG) on SiO$_2$/Si substrate with 90-nm thick SiO$_2$ (h_{SiO_2} = 90 nm) using an objective of NA = 0.45 and NA = 0.9. Notably, the objective of NA $\leq$ 0.55 is recommended for OC (λ) measurements to obtain better agreement between experimental and theoretical results [32]. In addition, when varying the thickness of SiO$_2$ covered on the Si wafer, the OC (λ) curve changes dramatically, as shown in Fig. 12.3B. Furthermore, the OC (λ) of 2DMs on the SiO$_2$/Si substrate is sensitive to the number of layers of 2DMs, which bridge the gap between OC (λ) and the determination of thickness of 2DMs. For example, as shown in Fig. 12.3C, as the thickness of *N*-layer graphene (*N*LG) increases, the OC maximum increases significantly once the NA and h_{SiO_2} are given. Therefore, once h_{SiO_2} is determined by OC [32], it is possible to distinguish the thickness of 2DMs by checking the agreements between the experimental and calculated OC (λ) based on the transfer-matrix method. The accuracy for the thickness identification of 2DM flakes is dependent on the OC (λ) difference between the flakes with adjacent number of layers. Generally, using OC (λ) can determine the number of layers of NLG up to $N = 8$.

For the effective measurement of the absorbance in semiconductor TMDs, it is common to use the transparent quartz substrate to measure the differential reflectance [34, 35], that is, the change in reflection intensity for 2DMs on quartz relative to that of the substrate, which can be defined by

$$\delta(\lambda) = R_{2DM+sub}(\lambda)/R_{sub}(\lambda) - 1. \tag{12.2}$$

The differential reflectance of a 2DM flake relative to a transparent substrate with refractive index of n_{sub} is related to the absorbance (A) of the 2DMs by $\delta(\lambda) = \frac{4}{n_{sub}^2 - 1} A(\lambda)$ [34]. Fig. 12.3D shows the schematic diagram for the incident and outgoing light within the multilayer medium of 2DMs deposited on a quartz substrate. Fig. 12.3E and F shows the corresponding differential reflectance of WS_2 and WSe_2 with the number of layers 1–5 [34], respectively. Distinct peaks represent the great absorbance related to the excitons. It is obvious that all the exciton peaks of WS_2 and WSe_2 exhibit a gradual blueshift with the thickness decreasing. Indeed, the excitonic absorption peaks A and B correspond to the direct transitions at the K (K') point and the energy between A and B arises from the spin-orbit interaction [13]. Besides, additional peaks can be observed, in which the C peak in WS_2 originates from the optical transition between the density of states peaks in the valence and conduction bands [36], while the A′ and B′ peaks of WSe_2 arise from the splitting of the ground and excited states of A and B transitions, respectively [34]. The differential reflectance is widely utilized to determine the exciton peak positions for semiconductors and their related vdWHs, including the intralayer and interlayer excitons [29, 34, 35].

12.3 Photoluminescence spectroscopy

When a semiconductor is excited by the external energy, the electrons within the valence band jump to the conduction band, leaving a hole within the valence band. Following the excitation, the electrons and holes can spontaneously decay to the band edges and recombine again to release the energy in the form of light. This process is called luminescence, including electroluminescence and PL. PL is one form of light emission as a result of a semiconductor excited by photon energy, which is related to its unique electronic band structure, lattice structure, defects, carrier transport, and so on [13, 34, 37, 38]. For a semiconductor exhibiting a large exciton binding energy, the excited electron will be attracted to a hole by the electrostatic Coulomb force to form an exciton, and its optical properties are dominated by excitonic effects.

PL spectroscopy has been extensively studied in various material systems to reveal their optoelectronic properties. In recent years, a series of fascinating optical properties, such as strong excitonic effects and valley polarization, have been extensively reported in 2DMs and their vdWHs, which can be directly revealed by PL spectroscopy and will be demonstrated in detail later [27–29, 39–41].

Most MX_2 undergo a transition from an indirect-gap semiconductor in the bulk form to a direct-gap semiconductor in the monolayer due to the absence of weak interlayer coupling in the monolayer [13]. Furthermore, the strong dimensionality confinement and reduced dielectric screening can greatly enhance the exciton binding energy, up to hundreds of meV [42, 43]. Thus, the few-layer MX_2 tend to exhibit strong excitonic effects, which can greatly modulate their optical properties, such as PL and optical absorption. The direct bandgap in monolayer TMD can significantly enhance its PL yield. For example, the surprising bright PL from monolayer MoS_2 (1LM) can be detected in contrast to that from bilayer MoS_2, as shown in Fig. 12.4A [13]. With increasing the number of layers of MoS_2 from 1 to 6, the quantum yield decreases monotonously, as depicted in the inset of Fig. 12.4A. The corresponding normalized PL spectra of one to six layered MoS_2 by the A exciton emission are depicted in Fig. 12.4B. The 1LM exhibit a single narrow PL profile at 1.90 eV; however, the two to six layered MoS_2 flakes show multiple emission peaks, A, B, and I, corresponding to two direct-gap electronic transitions at the K (K') point and an indirect-gap transition, respectively. As the number of layers increases, the peak I shifts to smaller energy and becomes less prominent. Similar results have been revealed in other MX_2, such as WS_2, WSe_2, and $MoTe_2$ [34, 35].

Apart from the strong excitonic effects in monolayer MX_2, the inversion symmetry breaking together with spin-orbit coupling (SOC) can lead to coupled spin and valley physics in monolayer group-VI dichalcogenides [44]. This makes it possible to control the spin and valley states, shedding light on the routine toward the integration of valleytronics and spintronics in these 2DMs. Taking 1LM as an example, Fig. 12.4C plots its schematic electronic band structure, in which the conduction and valence-band edges are located at the corners (K and K' points) of the 2D Brillouin zone (BZ). The two inequivalent valleys constitute a binary index for low-energy carriers. On the one hand, due to the D_{3h} symmetry of monolayer MX_2, the inversion symmetry is broken, which results in valley-dependent optical selection rules for interband transition at the K (K') point. On the other hand, the strong SOC originating from the d orbitals of the heavy metal atoms would lead to the splitting of the valence-band edge states. In addition, the time-reversal symmetry requires that the spin splitting at different valleys must be opposite, as elucidated in Fig. 12.4C. Such strong coupling between spins and valleys can be directly detected by optical pumping with circularly polarized light [39, 41], because the interband transitions in the vicinity of the K (K') point can exclusively couple to the right-(left)-handed circularly polarized light $\sigma^+(\sigma^-)$. In principle, $\sigma^+(\sigma^-)$ excitation light can generate $\sigma^+(\sigma^-)$ PL emission. However, the PL emission under circularly polarized excitation is not perfect circularly polarized light due to the intervalley scattering process. The degree of circular polarization for PL emission is commonly defined as

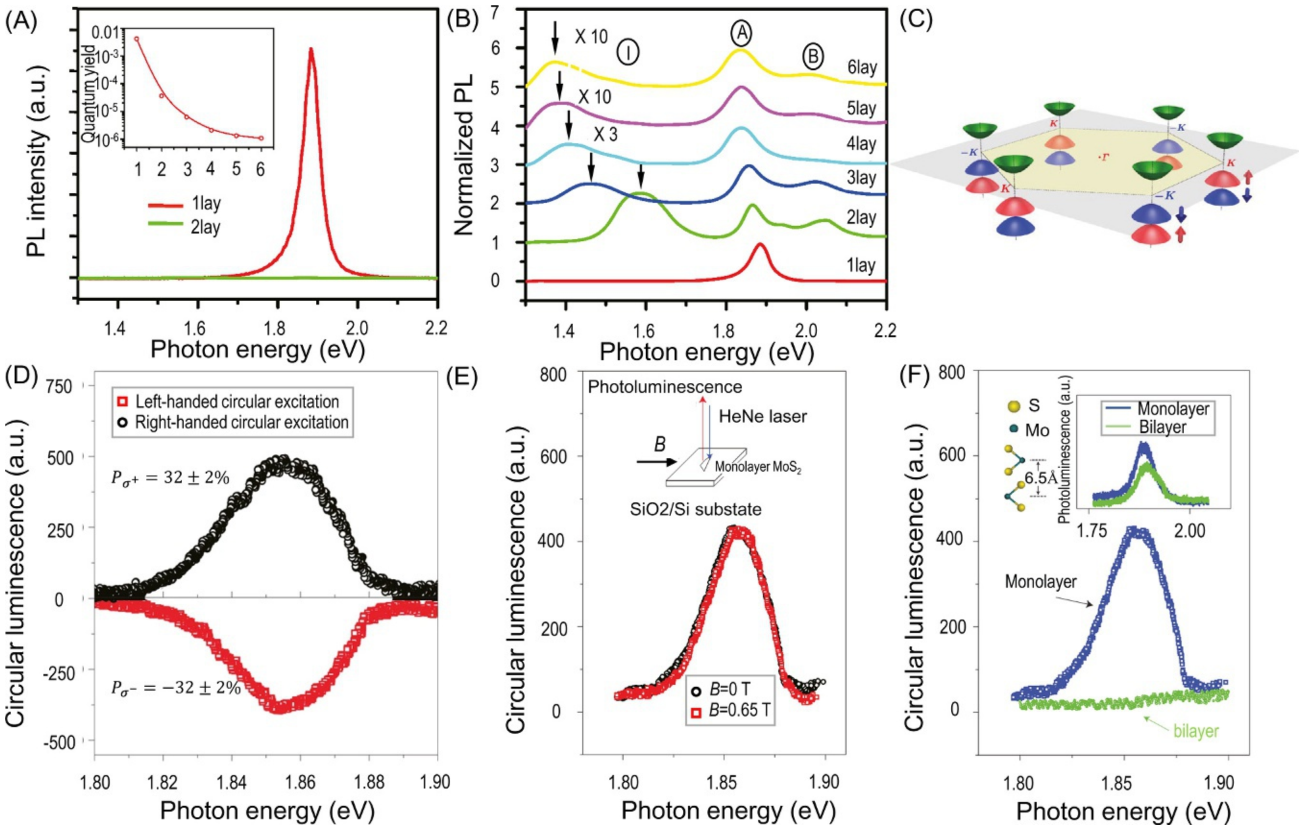

Fig. 12.4 See Figure legends on opposite page.

Continued

$$\rho = \frac{I(\sigma^{+}) - I(\sigma^{-})}{I(\sigma^{+}) + I(\sigma^{-})}, \tag{12.3}$$

where $I(\sigma^{\pm})$ is the left-/right-handed circular component intensity. Fig. 12.4D represents the circularly polarized PL spectra of 1LM under the σ^{+} and σ^{-} polarized excitations of 1.96 eV (near A exciton) at 10 K. The ρ for 1LM is ~0.3. The spin polarization mechanism of polarized PL can be excluded by the magnetic field-independent PL polarization shown in Fig. 12.4E. Otherwise, the spin polarization will process about the in-plane magnetic field and lead to decreased ρ. The valley polarization origin of such polarized PL can be further confirmed by a comparison of circular polarization of PL between the 1LM and bilayer MoS_2 (2LM). The preserved inversion symmetry in 2LM leads to a forbidden valley-dependent selection rule. Thus, the circular polarization of PL in 2LM is expected to be negligible, in good agreement with the experimental results, as shown in Fig. 12.4F.

In addition, abundant intriguing phenomena modified by defects, electronic doping, and lattice structure in semiconductor 2DMs have been reported recently. The neutral and charged defects in TMDs can bind the excitons to generate the so-called bound excitons [45]. Single-photon emission based on spatially localized excitons in TMD monolayers can be manipulated by electric and magnetic fields [46–48]. Electrical doping can efficiently control the neutral and charged excitons in monolayer semiconductor 2DMs [45]. All these extraordinary phenomena suggest interesting physics in 2DMs and a great potential of 2DMs in nanophotonics.

Furthermore, the optical properties and PL spectroscopy can be modulated by the band alignments of the constituents and the stacking order in vdWHs. As demonstrated in Section 12.1, the moiré superlattice can be naturally generated in twisted

Fig. 12.4 (A) PL spectra of monolayer and bilayer MoS_2 flakes in the range of 1.3–2.2 eV. The *inset* plots the quantum yield of 1–6L MoS_2. (B) Normalized PL spectra of 1–6L MoS_2 by the A emission peak. The spectra are scaled and offset for clarity and the scaling factors are shown. (C) Schematics of the band structure of 1LM at the K (K') point of BZ. (D) Polarization-resolved PL spectra under left-handed (σ^{+}) and right-handed (σ^{-}) circular excitations from a 1.96 eV laser at 10 K. (E) Circularly polarized components of PL spectra at zero and 0.65 T in-plane magnetic field. The *inset* shows the schematic configuration for the PL measurements. (F) Circularly polarized components of PL spectra from monolayer (*blue*) and bilayer (*green*) MoS_2. The *upper left inset* is the schematic of bilayer MoS_2 unit cell, while the *right upper inset* represents the PL spectra of monolayer (*blue*) and bilayer (*green*) MoS_2 under linearly polarized excitation of 1.96 eV at 10 K.

(A, B) Adapted from K.F. Mak, C. Lee, J. Hone, J. Shan, T.F. Heinz, Atomically thin MoS_2: a new direct-gap semiconductor, Phys. Rev. Lett. 105 (13) (2010) 136805, https://doi.org/10.1103/PhysRevLett.105.136805; (C) adapted from D. Xiao, G.-B. Liu, W. Feng, X. Xu, W. Yao, Coupled spin and valley physics in monolayers of MoS_2 and Other group-VI dichalcogenides, Phys. Rev. Lett. 108 (19) (2012) 196802, https://doi.org/10.1103/PhysRevLett.108.196802; (D–F) adapted from H. Zeng, J. Dai, W. Yao, D. Xiao, X. Cui, Valley polarization in MoS_2 monolayers by optical pumping, Nat. Nanotechnol. 7 (8) (2012) 490–493, https://doi.org/10.1038/nnano.2012.95.

systems or the vdWHs formed by constituents with nearly the same lattice constants, which periodically and laterally modulated the electronic and topographic structures [24]. For example, nanodot superstructures can be generated to confine the long-lived interlayer excitons, forming the so-called moiré excitons, as shown in Fig. 12.5A. The optical properties of moiré excitons can be constructed by moving adiabatically wave packets in the moiré potential. There are three kinds of high-symmetry sites (denoted as A, B, C sites) with threefold rotational ($\hat{C}_3$) symmetry preserved, in which the exciton wave packet (χ) is an eigenfunction of $\hat{C}_3$ rotation: $\hat{C}_3\chi_{A,s} = e^{-i\frac{2\pi}{3}s}\chi_{A,s}$, $\hat{C}_3\chi_{B,s} = e^{i\frac{2\pi}{3}s}\chi_{B,s}$, $\hat{C}_3\chi_{C,s} = \chi_{C,s}$, where s denoted the spin-valley index, $s = +(-)$ represents the exciton at the $K(-K/K')$ point with up (down) spin. Because the photons can only be convertible with excitons of the same rotational symmetry, the spin-up exciton wave packet at the A (B) site only couples to σ^+ (σ^-) polarized light while at the C site, light coupling is forbidden. The $\hat{C}_3$ symmetry also leads to energy extrema with energy variation up to ~100 meV, which makes it possible to trap the exciton into a moiré potential, as shown in Fig. 12.5A. The experimental signatures of the moiré excitons have been unveiled recently [27–29]. Due to strong valley polarization of the trapped interlayer excitons, the PL peak in heterobilayers should display large circular polarization. For example, in $MoSe_2$/WSe_2 heterobilayers, cocircularly polarized PL can be observed in the samples with $\theta = 57$ degrees and $\theta = 20$ degrees, while cross-circularly polarized PL is observed in that of $\theta = 2$ degrees, as shown in Fig. 12.5B–D. The features of moiré excitons can be further confirmed by the magneto-PL spectroscopy, in which all PL peaks experience Zeeman splitting under a nonzero magnetic field, as shown in Fig. 12.5E–G. The energies of the σ^+ and σ^- emission shift equally but in opposite directions. The energy difference between σ^+ and σ^- under the linearly polarized excitation would increase with increasing the magnetic field value. The extracted Landé g-factor of the moiré excitons are -15.89, -15.79, and 6.72 for the $MoSe_2$/WSe_2 heterobilayers with $\theta = 57$ degrees, $\theta = 20$ degrees, and $\theta = 2$ degrees, respectively, as demonstrated in Fig. 12.5H–J. The g-factor is similar for all the PL peaks in heterobilayers with similar twist angles [27]. The similar g-factors for heterobilayers with $\theta = 57$ degrees and $\theta = 20$ degrees arise from the similar valley pairings of the heterobilayers with twist angles in the vicinity of 60 and 21.8 degrees. However, due to the weaker optical dipole of the umklapp recombination at 21.8 degrees than that of the direct recombination at 0 and 60 degrees, the PL emission for heterobilayers with $\theta = 20$ degrees is much weaker than of $\theta = 2$ degrees and $\theta = 57$ degrees, in line with the experimental results depicted in Fig. 12.5B–D. In addition, Tran et al. have revealed that the energy spacing between the PL peaks from interlayer exciton of $MoSe_2$/WSe_2 heterobilayers is twisted-angle dependent, which is consistent with the calculations of trapped excitons confined within a moiré potential [28]. Jin et al. highlighted that the moiré exciton states in WSe_2/WS_2 with a small twist angle manifest as multiple emergent peaks around the A exciton of pristine WSe_2 and exhibit distinct gate-dependent behaviors from that of the A exciton in monolayer WSe_2 and heterobilayers with a large twist angle [29]. The experimental evidence of moiré excitons presents potential platforms to manipulate the excitons and moiré optics in vdWHs for nanophotonics and quantum information applications.

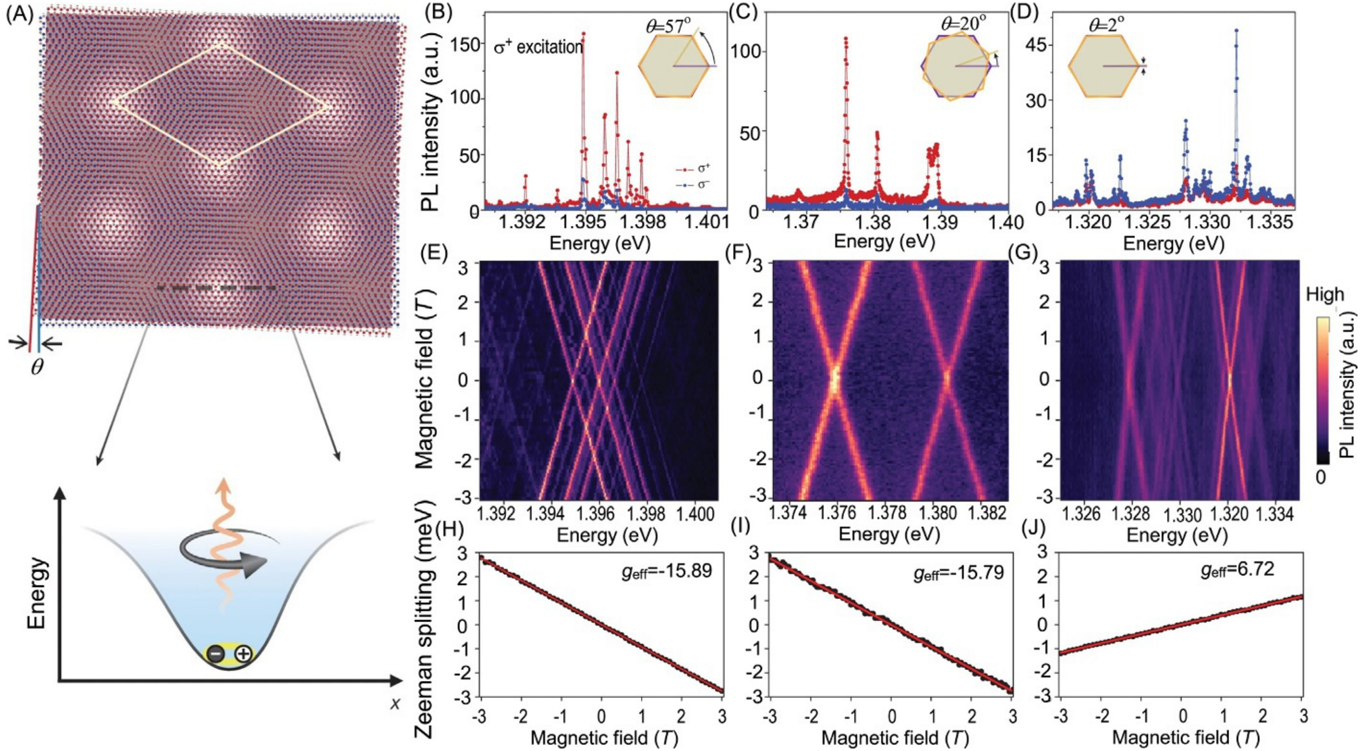

Fig. 12.5 (A) Schematic of moiré superlattice formed in a heterobilayer with θ and an exciton trapped in a moiré potential site. Helicity-resolved PL spectra of a trapped interlayer exciton of $MoSe_2/WSe_2$ heterobilayers with (B) $\theta = 57$ degrees, (C) $\theta = 20$ degrees, and (D) $\theta = 2$ degrees excited with σ^+ polarized light at 1.72 eV. The *insets* show their corresponding twist angles. (E–G) Total PL intensity with the change of magnetic field for the above three sample, respectively. (H–J) Zeeman splitting of the polarization-resolved PL as a function of the applied magnetic field for the above three samples, respectively.

Adapted from K.L. Seyler, P. Rivera, H. Yu, N.P. Wilson, E.L. Ray, D.G. Mandrus, J. Yan, W. Yao, X. Xu, Signatures of moiré-trapped valley excitons in $MoSe_2/WSe_2$ heterobilayers, Nature 567 (7746) (2019) 66–70, https://doi.org/10.1038/s41586-019-0957-1.

12.4 Rayleigh scattering

Optical spectroscopy associated with light scattering has been proved to be a fast, sensitive, and nondestructive tool in the characterization and investigation of physical properties in 2DMs [3, 49]. According to energy transfer in light-matter interactions, light scattering can be divided into elastic and inelastic, which corresponds to Rayleigh scattering and Raman/Brillouin scattering. Compared with the minority inelastic scattering photons, the number of elastically scattered photons is much larger. As the 2DMs are usually deposited on SiO_2/Si substrate, similar to the OC of 2DMs shown in Fig. 12.2A, the Rayleigh scattering intensity from the 2DMs depends on the complex refractive index of each medium, multiple reflection at the interfaces, and the interference within the multilayer containing air, 2DMs, and substrate. Therefore, the Rayleigh scattering contrast from 2DMs on substrate relative to that from substrate, which is defined by Eq. (12.1), provides an effective means to identify the number of layers of 2DMs and their dielectric constants [50, 51]. Fig. 12.6A and B shows one typical optical image of 1–3LG and 6LG deposited on the SiO_2/Si substrate ($h_{SiO2} = 300$ nm) and the corresponding Rayleigh mapping under backscattering configuration with 633 nm excitation, respectively. The Rayleigh signal intensity increases as the number of layers N increases. Similar to the OC, the theoretical Rayleigh contrast can also be

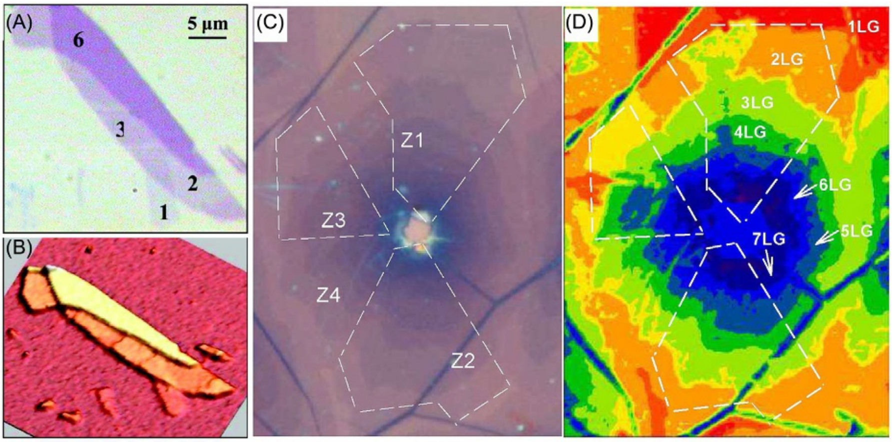

Fig. 12.6 (A) Optical image of 1–3LG and 6LG. (B) The corresponding Rayleigh mapping for the samples in (A) under 633 nm excitation. (C) Optical image of a CVD grown MLG flake. (D) The corresponding Rayleigh mapping for flake in (C) under 532 nm excitation. Stronger Rayleigh intensity is represented by *darker color*.
(A, B) Adapted from C. Casiraghi, A. Hartschuh, E. Lidorikis, H. Qian, H. Harutyunyan, T. Gokus, K.S. Novoselov, A.C. Ferrari, Rayleigh imaging of graphene and graphene layers, Nano Lett. 7 (9) (2007) 2711–2717, https://doi.org/10.1021/nl071168m; (C, D) adapted from J.-B. Wu, H. Wang, X.-L. Li, H. Peng, P.-H. Tan, Raman spectroscopic characterization of stacking configuration and interlayer coupling of twisted multilayer graphene grown by chemical vapor deposition, Carbon 110 (2016) 225–231, https://doi.org/10.1016/j.carbon.2016.09.006.

calculated based on the transfer-matrix method once the complex refractive index of each medium is known [50]. The number of layers of 2DMs can be determined by comparing the experimental Rayleigh contrast value with the theoretical one. Fig. 12.6C and D shows the optical image of a chemical vapor deposition (CVD)-grown multilayer graphene (MLG) flake and the corresponding Rayleigh contrast [51], in which the Rayleigh contrast increases with *N* increasing. The *N*LG in each region can be identified by the color in the Rayleigh contrast mapping, as shown in the image.

Although the methods to determine the number of layers of 2DMs by Rayleigh contrast and OC are similar with each other, the spatial resolution of Rayleigh contrast can be down to ~1 μm because laser excitation is used. As the measured Rayleigh contrast is equal to a monochromatic OC with the same excitation wavelength as the laser source for the Rayleigh contrast, one can choose an optimal wavelength at the OC maximum to achieve better signal-to-noise ratio for the Rayleigh contrast. For the number of layers identification, it would be better to choose a laser wavelength that makes Rayleigh contrast sensitive to the number of layers of 2DMs.

12.5 Raman spectroscopy

Raman scattering is one kind of inelastic scattering, in which the energy shift between the incident and scattered light corresponds to the energy of quasiparticles or elementary excitation (e.g., phonons) involved in the process of light-matter interactions. As a consequence, Raman spectroscopy is extensively utilized to explore the fundamental physics in a material, such as lattice structure and symmetry, lattice vibrations, defects, electronic band structure, interlayer coupling, electron-phonon coupling (EPC), etc., especially in 2DMs [3, 5, 7, 49, 52, 53]. Here, we focus on the Raman scattering of phonons in 2DMs, showing three typical examples of Raman spectroscopy study in 2DMs: (a) Raman spectroscopy in pristine 2DMs by taking $MoTe_2$ as a prototype [54]; (b) Raman spectroscopy of twisted 2DMs, with twisted bilayer MoS_2 (tBLM) as an example [25]; and (c) Raman spectroscopy of vdWHs by taking the hBN/WS_2 heterostructure as a model [55], which illustrates the influences of number of layers, stacking order, and interlayer/interfacial coupling on the Raman spectroscopy of 2DMs and vdWHs. The analysis here can be extended to other 2DMs and related vdWHs, paving the way to their characterizations and investigations.

12.5.1 Raman spectroscopy in pristine 2DMs

Monolayer 2DMs can be stacked layer by layer in a specific way to form multilayer 2DMs, which possess strong in-plane bonds and weak vdW interlayer coupling. Thus, the Raman spectroscopy of *N*L-2DMs ($N > 1$) consists of Raman modes in low- and high-frequency regions, in which the low-frequency Raman modes are induced by the relative motions of adjacent layers (so-called interlayer modes), while the high-frequency modes result from the relative motions of the atoms in a rigid layer (so-called intralayer modes). There are two kinds of interlayer modes, shear (S) and layer

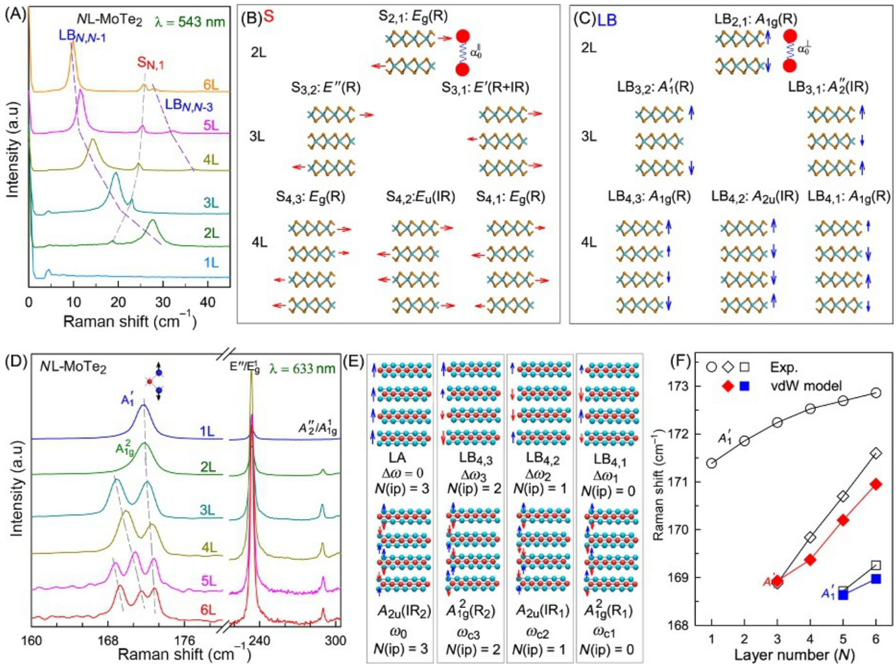

Fig. 12.7 (A) The Stokes Raman spectra of 1–6L $MoTe_2$ in the region of 0–45 cm^{-1} under the excitation at 543 nm. Symmetries, Raman activities, and normal mode displacements for the (B) S and (C) LB modes in 2–4L 2H-$MoTe_2$. R represents Raman active and IR represents infrared active. The *arrows* indicate the vibrational direction of the corresponding layers and the length represents the amplitude of the displacements. (D) The Raman spectra of 1–6L $MoTe_2$ in the range of 160–305 cm^{-1} under the excitation at 633 nm. (E) Schematic of the vdW model for Davydov splitting in 4L $MoTe_2$. N(ip) is the number of the in-phase vibration interfaces. (F) The experimental frequency (*open diamonds* and *squares*) of each Davydov entity of $A_1'(A_{1g})$ modes in 3–6L $MoTe_2$ and the corresponding calculated frequency (*solid diamonds* and *squares*) based on the experimental value of the highest-frequency component and vdW model. The experimental frequencies of the $A_1'(A_{1g})$ modes in 1–2L $MoTe_2$ are also plotted.
(A, D–F) Adapted from Q.J. Song, Q.H. Tan, X. Zhang, J.B. Wu, B.W. Sheng, Y. Wan, X.Q. Wang, L. Dai, P.H. Tan, Physical origin of Davydov splitting and resonant Raman spectroscopy of Davydov components in multilayer $MoTe_2$, Phys. Rev. B 93 (11) (2016) 115409, https://doi.org/10.1103/PhysRevB.93.115409.

breathing (LB) modes, which correspond to the interlayer vibrations parallel and perpendicular to the 2D basal plane, respectively. The S mode is also referred to as the C mode in MLG [20, 56, 57] as it provides a direct probe for the interlayer *coupling*. Other denotations, such as SM, B, and LBM are also introduced by different groups. The frequencies of S and LB modes are both dependent on the number of layers due to the interlayer characteristics, as depicted in Fig. 12.7A. For these interlayer modes, the relative vibrations between the atoms within each rigid layer can be negligible; thus, one rigid layer can be treated as a ball and only the nearest interlayer S/LB coupling

($\alpha_0^{\parallel}$ / $\alpha_0^{\perp}$) between adjacent balls is considered, as shown in Fig. 12.7B and C. This model is known as the linear chain model (LCM) [20, 56–58]. The frequency of the S and LB modes can be calculated by solving the following $N \times N$ (tridiagonal) dynamics matrix [3, 20, 56, 57]:

$$\omega_i^2 \mathbf{u}_i = \frac{1}{2\pi^2 c^2 \mu} \mathbf{D} \mathbf{u}_i, \tag{12.4}$$

where $\mathbf{u}_i$ is the eigenvector of the mode i with frequency ω_i, μ is the mass of single rigid layer per unit area, $c = 3.0 \times 10^{10}$ cm s^{-1} is the speed of light, and $\mathbf{D}$ is the S or LB part of the force constant matrix. Thus, the frequencies of the corresponding $\mathrm{S}_{N,\ N-i}$ and $\mathrm{LB}_{N,N-i}$ modes can be given by [3, 5, 58]

$$\begin{aligned} \omega(\mathrm{S}_{N,N-i}) &= \frac{1}{\pi c}\sqrt{\alpha_0^{\parallel}/\mu}\sin\left(\frac{i\pi}{2N}\right), \\ \omega(\mathrm{LB}_{N,N-i}) &= \frac{1}{\pi c}\sqrt{\alpha_0^{\perp}/\mu}\sin\left(\frac{i\pi}{2N}\right), \end{aligned} \tag{12.5}$$

where $i = 1, 2, \ldots, N-1$. There are $N-1$ LB and $N-1$ doubly degenerate S modes for the in-plane isotropic NL-2DMs, where N is the number of layers and i is the number of phonon branches. The $i = N-1$ branches, that is, $\mathrm{S}_{N,1}$ and $\mathrm{LB}_{N,1}$ modes, correspond to the highest-frequency S and LB modes, respectively. The calculated frequencies of the S and LB modes in $\mathrm{MoTe_2}$ as a function of N are in good agreement with the experimental ones. The corresponding ith displacement eigenvector $\nu_j^{(i)}$ is given by

$$\nu_j^{(i)} = \cos\left[\frac{i(2j-1)\pi}{2N}\right], \tag{12.6}$$

where j labels the jth layer. For NL-2DMs with in-plane anisotropy, there are $N-1$ LB modes, similar to that in in-plane isotropic NL-2DMs. However, as the two axes in the basal 2D plane are not equal in anisotropic NL-2DMs, for example, $\mathrm{ReS_2}$, there are $2(N-1)$ nondegenerate S modes, named as $\mathrm{S}^x_{N,N-i}$ and $\mathrm{S}^y_{N,N-i}$ modes [59].

Fig. 12.7B and C depicts the layer displacements of the S and LB modes in 2–4L $\mathrm{MoTe_2}$. Because the ONL and ENL $\mathrm{MoTe_2}$ belong to D_{3h} and D_{3d} symmetries, respectively, the interlayer modes in ONL and ENL $\mathrm{MoTe_2}$ can be represented by $\frac{N-1}{2}(A_1'(\mathrm{R}) + E''(R) + A_2''(\mathrm{IR}) + E'(\mathrm{R+IR}))$ and $\frac{N}{2}(A_{1\mathrm{g}}(\mathrm{R}) + E_{\mathrm{g}}(\mathrm{R})) + (\frac{N}{2}-1)(A_{2\mathrm{u}}(\mathrm{IR}){+}E_{\mathrm{u}}(\mathrm{IR}))$, respectively. R and IR represent Raman active and infrared active, respectively. The corresponding Raman/infrared activity for $\mathrm{S}_{N,N-i}$ and $\mathrm{LB}_{N,\ N-i}$ modes in 2–4L $\mathrm{MoTe_2}$ is indicated in Fig. 12.7B and C, which suggests that $\mathrm{S}_{N,\ N-i}$ $(i = N-1, N-3, N-5, \ldots)$ and $\mathrm{LB}_{N,N-i}$ $(i = 1, 3, 5, \ldots)$ modes are Raman active, in line with the experimental results in Fig. 12.7A [54]. Due to the in-plane isotropy in $\mathrm{MoTe_2}$, the $N-1$ doubly degenerate S modes belong to E symmetry, while the

$N - 1$ LB modes belong to A symmetry. It is also the case for all in-plane isotropic MX_2. Thus, the Raman-active S modes can be detected under both parallel and cross-polarization configurations, while the Raman-active LB modes can only be observed under the parallel polarization configuration. This provides one method to distinguish the S and LB modes. The detailed assignments of the S and LB modes and demonstrations for their measurements in typical 2DMs can be found in [3].

The weak interlayer coupling can also influence the intralayer modes. Fig. 12.7D plots the Raman spectra of 1–6L $MoTe_2$ in the region of intralayer modes. Only two intralayer modes can be detected in 1L $MoTe_2$, which correspond to A'_1 ($\sim$170 cm^{-1}) and E' ($\sim$233 cm^{-1}) intralayer phonons. For multilayer $MoTe_2$, the A'_1 (A_{1g}) and E' (E_g) modes in ONL (ENL) $MoTe_2$ can be observed, corresponding to the A'_1 and E' modes in 1L $MoTe_2$, respectively. An additional mode at $\sim$291 cm^{-1} corresponding to the Raman-inactive B_{2g} mode in 1L $MoTe_2$ can be probed due to the reduced symmetry in multilayer $MoTe_2$ [54]. One intriguing phenomenon of peak splitting is observed for A'_1-like modes in NL $MoTe_2$, in which the number and frequency of the components depend on N due to interlayer coupling. In principle, when considering the nearest interlayer coupling, the intralayer modes in $MoTe_2$ would exhibit varied frequency when the two nearest Te atoms in adjacent layers exhibit in-phase and out-of-phase vibrations. The out-of-phase vibration between the two nearest Te atoms tends to raise the frequency compared with the in-phase vibration, resulting in the so-called Davydov splitting [54]. This can be well reproduced by the vdW model, as demonstrated in detail later [54]. Assuming the frequency of the isolated entity and the uncoupled entity displaying in-plane vibration is ω_0; the frequency of coupled entity displaying out-of-phase vibration is ω_c; and the coupling frequency is $\Delta\omega$, these three frequencies are associated by the relation of $\omega_c^2 = \omega_0^2 + \Delta\omega^2$. Thus, for NL ($N > 1$) $MoTe_2$, the intralayer modes would split into N components. However, the number of components that can be detected in the Raman spectroscopy depends on their Raman activity, the splitting frequency, and the spectral resolution of the Raman system for measurements. As shown in Fig. 12.7D, the Davydov splitting is only clear for A'_1-like modes. The A'_1 mode in 1L $MoTe_2$ would split into N A'_1-like modes, represented by $\frac{N+1}{2}A'_1(\mathrm{R})+\frac{N-1}{2}A''_2(\mathrm{IR})$ for ONL $MoTe_2$ and $\frac{N}{2}A_{2u}(\mathrm{IR})+\frac{N}{2}A^2_{1g}(\mathrm{R})$ for ENL $MoTe_2$. Thus, it is expected to observe $\frac{N+1}{2}$ and $\frac{N}{2}$ Davydov components in ONL and ENL $MoTe_2$, respectively, in good agreement with the experimental results shown in Fig. 12.7D. The atomic displacements of A'_1-like modes and LB modes for 4L $MoTe_2$ are elucidated in Fig. 12.7E, together with the number of the in-phase vibration interfaces (N(ip)) denoted. When taking detailed consideration of the frequency of the Davydov components, the coupling frequency $\Delta\omega$ can be closely related to the frequency of LB modes with the same N(ip) because the atomic displacements of the A'_1-like modes are perpendicular to the basal plane. The frequency of the A_{2u}(IR) mode is that of the uncoupled entities, ω_0, and the frequencies of the other three modes (ω_{ci}, $i = 1, 2, 3$) can be calculated. This is the so-called vdW model. According to the Raman-active Davydov components with the highest frequency of 3–6L $MoTe_2$ and vdW model, the corresponding frequency of other Davydov components can be deduced (solid diamonds and squares), in line with the experimental results (open diamonds and squares), as shown in Fig. 12.7F. Notably, different Davydov components would exhibit varied resonance profiles because of their different EPC. Therefore, it is essential to choose an appropriate excitation energy to measure the Davydov components [54]. Similar Davydov splittings have been observed in other MX_2 [60, 61], such as $MoSe_2$ and WS_2. The above vdW model can be extended to reproduce the Davydov splitting associated with S and LB modes in other 2DMs [62].

12.5.2 Raman spectroscopy of twisted 2DMs

As referred to earlier, the twisted stacking at the interface of the twisted 2DMs can generate the moiré superlattice to modulate the phonon behaviors of the constituents. tBLM can be treated as a simple model system to introduce the modified Raman spectra in twisted 2DMs [25]. There exist moiré superlattices in tBLM, whose lattice constant can be represented by $L^M = a/[2(\sin(\theta/2))]$, where a is the lattice constant of the 1LM. Accordingly, the corresponding reciprocal lattices can be constructed. Fig. 12.8A shows the reciprocal lattices corresponding to the moiré superlattices of tBLM with $\theta = 10.99$ degrees, in which the large blue and orange hexagons are the Brillouin zones (BZs) of the top and bottom monolayers, respectively. Meanwhile, the red-dashed hexagons correspond to the Wigner-Seitz cells in reciprocal space related to the moiré superlattices. The basic vectors ($\boldsymbol{g}$ and $\boldsymbol{g}'$) of the moiré reciprocal superlattice can be evaluated by the relative vectors between the reciprocal lattice vectors of the top and bottom monolayers, giving an absolute value of $|\boldsymbol{g}| = |\boldsymbol{g}'| = 2b\sin(\theta/2)$. There are many lattice vectors of moiré reciprocal superlattices within the BZ of the monolayer constituent, because its basic vector is smaller than that of 1LM, as Γ_{j1} ($j = 1, 2, \ldots, 6$) labeled for the moiré reciprocal superlattice in Fig. 12.8A. With changing θ, the trajectory of $\boldsymbol{g}$ for the moiré reciprocal superlattice in the BZ of the monolayer constituent can be obtained, as the dashed line shown in Fig. 12.8B. Three representative basic vectors of the moiré reciprocal superlattice, that is, $\boldsymbol{g}_i$ ($i = 1$, 2, 3) corresponding to 30 degrees $- \theta_1$, 30 degrees $- \theta_2$, and 30 degrees are also depicted in Fig. 12.8B. Notably, the moiré superlattice with 30 degrees $- \beta$ and 30 degrees + β (0 degrees $< \beta <$ 30 degrees) are two commensurate partners.

In twisted bilayer 2DMs, the periodic modulation of moiré superlattices on the interlayer interactions leads to not any overall restoring force for the in-plane displacements when θ is away from 0 or 60 degrees (~5–55 degrees). Thus, the S modes locate at almost zero wave number and cannot be observed in low-frequency Raman spectroscopy. As shown in Fig. 12.8C, the $S_{2,1}$ modes are absent in the Raman spectra of tBLMs when $\theta \neq 0$ degrees and $\theta \neq 60$ degrees, further confirming that the interlayer S coupling is not enough to produce an overall restoring force between the two monolayer constituents. Similar results have been observed in twisted multilayer graphenes (tMLGs) [3, 5, 20, 63] and twisted bilayer TMDs [18, 64, 65]. In contrast, the $LB_{2,1}$ modes are present with frequencies close to those in 2H- and 3R-stacked 2LMs, which can be ascribed to the comparability between interfacial LB coupling and interlayer LB coupling with pristine 2LM. The close frequency of LB modes in tBLMs (0 degrees $< \theta <$ 60 degrees) to those in 2H-/3R-stacked 2LM in Fig. 12.8C confirms the good LB coupling between the two monolayer

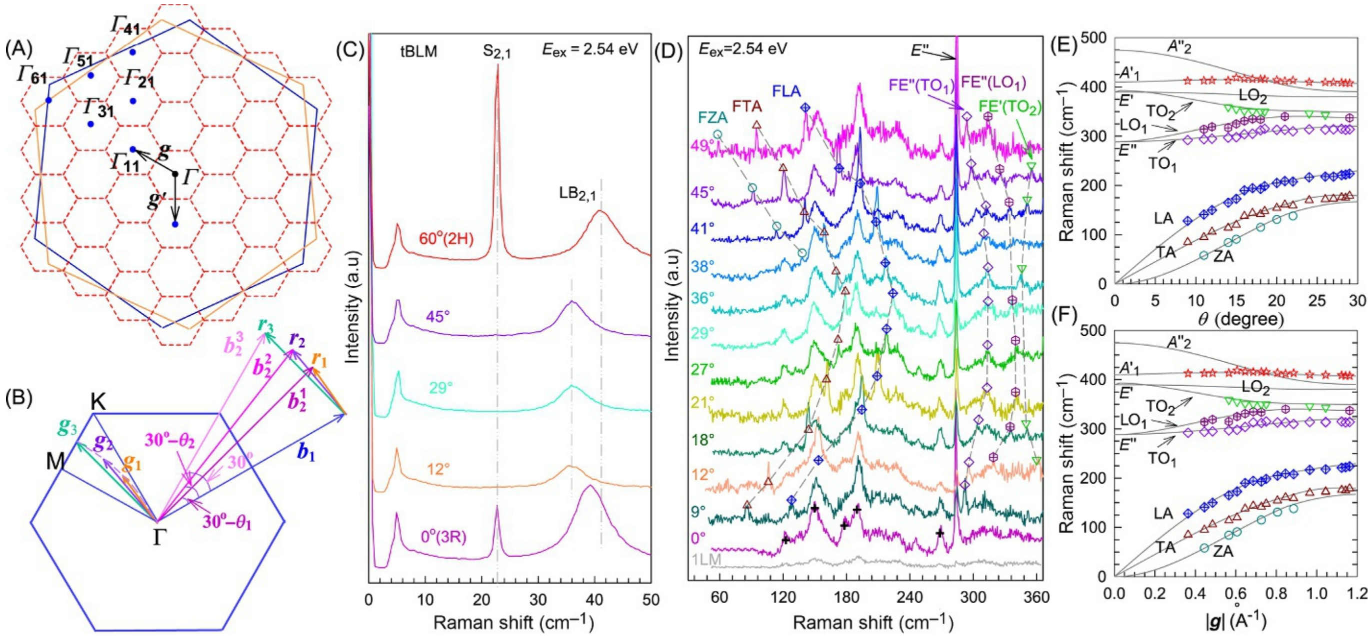

Fig. 12.8 (A) The reciprocal lattice of tBLM with $\theta = 10.99$ degrees; the *large blue* and *orange hexagons* represent the first BZ of the top and bottom MoS_2 layers, respectively. The *dashed* (*red*) *hexagons* are the Wigner-Seitz cells of the reciprocal lattices corresponding to the moiré superlattices. (B) Schematic diagram of moiré basic vectors ($\boldsymbol{g}_i$, $i = 1, 2, 3$) corresponding to 30 degrees $- \theta_1$, 30 degrees $- \theta_2$, and 30 degrees. (C) The Stokes Raman spectra of tBLMs with different θ in the low-frequency region. (D) The Raman spectra of tBLMs with θ ranging from 9–49 degrees in the region of 50–365 cm^{-1}, with the corresponding Raman spectra of 1LM and 3R-stacked BLM ($\theta = 0$ degrees) shown together. The calculated and experimental frequencies of moiré phonons dependent on (E) θ and (F) $|\boldsymbol{g}|$. The *solid gray lines* are the calculated phonon frequencies by the interpolation between those along the Γ-M and Γ-K directions in 1LM; the *scattered symbols* are the experimental data. Adapted from M.-L. Lin, Q.-H. Tan, J.-B. Wu, X.-S. Chen, J.-H. Wang, Y.-H. Pan, X. Zhang, X. Cong, J. Zhang, W. Ji, P.-A. Hu, K.-H. Liu, P.-H. Tan, Moiré phonons in twisted bilayer MoS_2, ACS Nano 12 (8) (2018) 8770–8780, https://doi.org/10.1021/acsnano.8b05006.

MoS_2 constituents, which is essential for the generation of moiré superlattices. In addition, according to the relative intensity between the $S_{2,1}$ and $LB_{2,1}$ modes [64], the tBLMs tend to exhibit 3R and 2H stacking when $\theta = 0$ degrees and $\theta = 60$ degrees, respectively.

In principle, the moiré superlattices are expected to result in phonon folding effects in tBLMs, in which the off-center phonons in the monolayer constituents linked with the corresponding reciprocal lattice vectors can be folded back to the BZ center of 1LM. Indeed, it was found that the periodic potential from moiré superlattice can modify the phonon properties of its monolayer constituents to generate the Raman modes related to moiré phonons [25]. As shown in Fig. 12.8D, a series of additional Raman modes are probed in tBLMs, with frequency monotonously changing for 0 degrees $< \theta < 30$ degrees and 30 degrees $< \theta < 60$ degrees, in coincidence with the case for the moiré superlattice. Based on the theory-experiment comparison from low to high frequency, the six series of θ-dependent Raman modes can be distinguished as the moiré phonons related to ZA, TA, LA, $E''(TO_1)$, $E''(LO_1)$, and $E'(TO_2)$ phonon branches in 1LM. They are the phonons *folded* back to the BZ center, denoted as FZA, FTA, FLA, $FE''(TO_1)$, $FE''(LO_1)$, and $FE'(TO_2)$, respectively. The frequencies of all the observed moiré phonon modes as a function of θ are plotted in Fig. 12.8E. The corresponding phonon branches of 1LM can be obtained according to $|\boldsymbol{g}| = 2b\sin(\theta/2)$, as elucidated in Fig. 12.8F, showing good agreement with the calculated phonon branches by the interpolation between those along the Γ-M and Γ-K directions in 1LM [25]. It should be noted that the Raman modes related to moiré phonons in tBLM would be greatly enhanced when the excitation energy is close to the C exciton energy [25]. Thus, the moiré phonon modes in all tBLMs can be observed with one excitation laser.

The above analysis can be extended to other twisted bilayer systems. Indeed, the θ-dependent Raman modes in twisted bilayer graphenes, which were previously assigned to rich resonance effects [66], are actually corresponding to the moiré phonon modes [25]. Besides, the moiré superlattices are also present in vdWHs formed by two constituents with nearly the same lattice constant, and thus moiré phonon modes are expected in these vdWHs [67]. Interestingly, reconstructions of the moiré superlattice are observed in twisted bilayers with small twist angles [68–70], in which many fascinating phonon properties are discovered, such as phonon renormalization due to the ultra-strong coupling between different phonon modes [71] and localization of lattice dynamics with the presence of strain solitons [72].

Twisted bilayers are the simplest prototype of twisted 2DMs. With increase of the number of layers of twisted 2DMs, a large family of twisted 2DMs can be generated, that is, $t(m+n+\cdots)$L-2DMs ($N = m+n+\cdots$), in which an even wider range of properties is accessible. The above analysis of the moiré phonons is also applicable in these complex twisted multilayer 2DMs, which are sensitive to the twist angle and moiré superlattice. Besides, the interlayer modes and nonfolded intralayer modes in twisted multilayer 2DMs are dependent on the interfacial coupling between the constituents. For interlayer modes, the negligible interfacial shear (S) coupling leads to the localization of the S modes within its constituents, while the remarkable LB coupling gives rise to collective vibration of all the stacking layers for the LB modes [3, 18], similar to those in twisted bilayer 2DMs. The effects of the interfacial and interlayer coupling on the nonfolded intralayer modes should also be divided into two categories according to the vibration directions [73]. For nonfolded in-plane intralayer modes, the vibrations are localized within the constituents of twisted multilayer 2DMs because of the negligible interfacial S coupling at the interface. Thus, the spectral profile of nonfolded in-plane intralayer modes can be fitted by those of the corresponding modes of its constituents. In contrast, because the interfacial LB coupling at the interface is comparable to the interlayer coupling within the constituents, the number of the Davydov entities of the nonfolded out-of-plane modes depends on the number of stacking layers (i.e., N) of the whole $t(m+n+\cdots)$L-2DMs. The Davydov splitting of the intralayer modes in $t(m+n+\cdots)$L-2DMs is quantitatively reproduced by the vdW model based on the frequencies of the corresponding LB modes, as elucidated in Section 12.5.1. As the interfacial LB coupling is independent of the large twist angle, the Davydov splitting of the nonfolded out-of-plane modes is also not sensitive to the twist angle. However, the moiré superlattice with different twist angles will impose varied modulation on electron-phonon coupling. Thus, the relative Raman intensity between different Davydov entities significantly varies with the twist angle. Notably, in order to resolve all the Davydov entities of the nonfolded out-of-plane intralayer modes, high-resolution resonance Raman spectroscopy at low temperature is always necessary [73].

12.5.3 Raman spectroscopy in vdWHs

As demonstrated in Section 12.5.2, one can infer that the S modes in twisted 2DMs are confined within the constituents, while the LB modes in twisted 2DMs are from the collective vibrations of all the stacking layers. Similar phenomena are observed in vdWHs consisting of different 2DMs [3, 55, 74]. Setting the hBN/WS_2 formed by n-layer hBN (nL-hBN) and m-layer WS_2 (mLW), that is, nL-hBN/mLW as a prototype, the peak position and EPC in vdWHs are demonstrated in detail. Fig. 12.9A displays the Raman spectra of 39L-hBN/3LW excited by a laser in the range of 2.41–2.81 eV, together with the Raman spectrum of the stand-alone 3LW flake under excitation at 2.71 eV. Similar S modes can be observed in stand-alone 3LW flakes and 39L-hBN/3LW, confirming the confinement of S modes within the constituents in vdWHs. Compared with the Raman spectrum of the stand-alone 3LW flake, many new LB modes are emergent, which can be reproduced by the LCM with interlayer coupling within the constituents and interfacial coupling between the constituents considered [55]. According to the peak position of the observed LB modes, the interlayer coupling of hBN ($\alpha^{\perp}$(BN)) and the interfacial coupling between hBN and WS_2 ($\alpha^{\perp}$(I)) constituents can be obtained. All the observed LB modes can be well reproduced and assigned by these fitted force constants, independent of the stacking order, and twist angle due to the large mismatch of lattice constants between hBN and WS_2. As the LB modes in nL-hBN/mLW can be well distinguished, even n is up to tens or hundreds of layer thickness, the LB modes exhibit 3D features [55].

Interestingly, all the observed LB modes in hBN/WS_2 are significantly enhanced when the excitation energy approaches the C exciton energy of the corresponding stand-alone WS_2 flake, as demonstrated in Fig. 12.9A and B. Furthermore, the resonance profile of these LB modes is similar to the S and LB modes in the

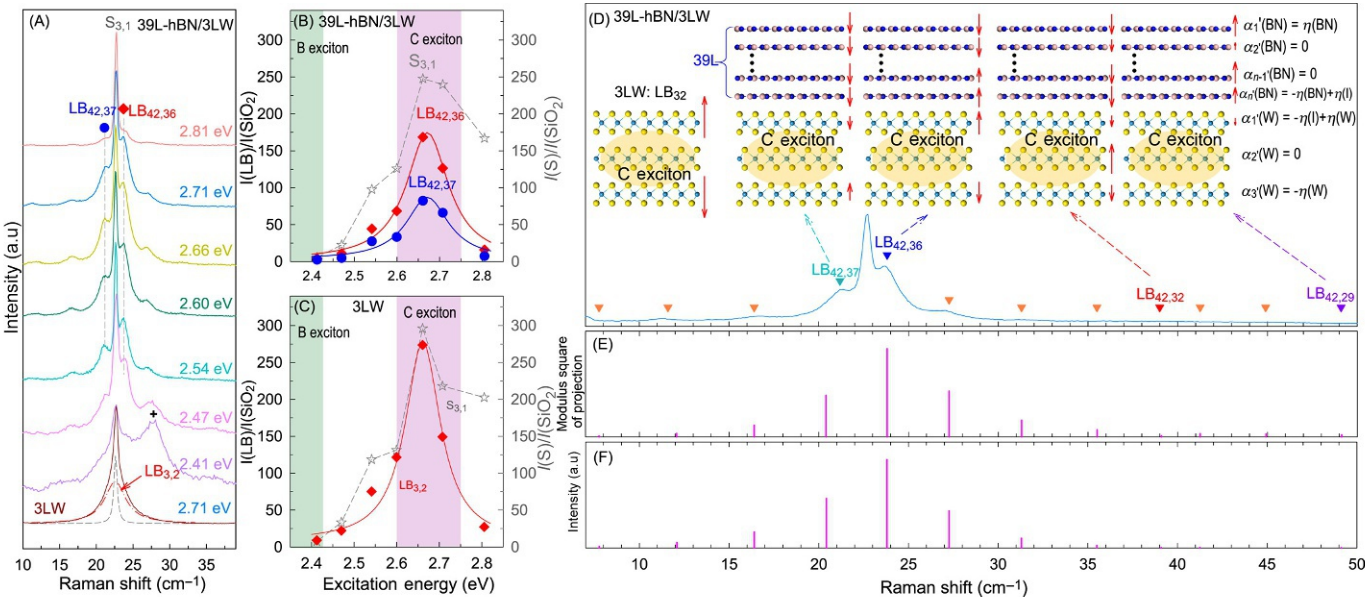

Fig. 12.9 (A) Raman spectra of 39L-hBN/3LW excited by E_{ex} ranging from 2.41 to 2.81 eV, together with the Raman spectrum of a stand-alone 3LW excited at 2.71 eV. The *gray dash* and *red dash-dot lines* plot the lineshape of $\mathrm{S}_{3,1}$ and $\mathrm{LB}_{3,2}$ modes in the stand-alone 3LW flake. The resonant profiles of (B) $\mathrm{LB}_{42,36}$ (*red diamonds*) and $\mathrm{LB}_{42,37}$ (*blue circles*) and $\mathrm{S}_{3,1}$ modes (*gray stars*) in 39L-hBN/3LW, (C) $\mathrm{LB}_{3,2}$ (*red diamonds*) and $\mathrm{S}_{3,1}$ (*gray stars*) in 3LW flake. (D) Raman spectroscopy of 39L-hBN/3LW in the region of 5–50 cm^{-1} and the normal mode displacements (*red arrows*) of $\mathrm{LB}_{42,37}$, $\mathrm{LB}_{42,36}$, $\mathrm{LB}_{42,32}$, $\mathrm{LB}_{42,29}$ modes, together with that of $\mathrm{LB}_{3,2}$ in a stand-alone 3LW flake. The *triangles* are the expected LB modes based on LCM. $\alpha_i'(\mathrm{BN})$ $(i = 1, 2, \ldots, n)$ and $\alpha'_j(W)(j = 1, 2, 3)$ are the polarizability derivatives of the entire layer i from the hBN constituent and layer j from the WS_2 constituent related to the displacement in the z-direction. (E) The modulus square of the projection from wave function of different LB modes in 39L-hBN/3LW onto that of the $\mathrm{LB}_{3,2}$ mode in a stand-alone 3LW flake. (F) The relative intensity of LB modes in 39L-hBN/3LW according to the interlayer bond polarizability model.

Adapted from M.-L. Lin, Y. Zhou, J.-B. Wu, X. Cong, X.-L. Liu, J. Zhang, H. Li, W. Yao, P.-H. Tan, Cross-dimensional electron-phonon coupling in van der Waals heterostructures, Nat. Commun. 10 (1) (2019) 2419, https://doi.org/10.1038/s41467-019-10400-z.

corresponding stand-alone WS_2 flake, as elucidated in Fig. 12.9C. Because the hBN/WS_2 heterostructure is classified into type-I vdWH based on the band alignment of hBN and WS_2 [55], the electronic states related to the C exciton of 3LW flakes are confined within the few-layer WS_2, displaying 2D features. Therefore, the resonance profile of LB modes in hBN/WS_2 similar to that in the corresponding WS_2 flakes implies the peculiar coupling between the 2D electrons and 3D LB phonons [55]. Such cross-dimensional EPC can be understood by a microscopic picture mediated by the interfacial coupling and the interlayer bond polarizability model in vdWHs. The Raman intensity of LB modes in vdWHs is associated with the EPC strength, which is directly related to their vibration displacements (Fig. 12.9D) within the first-order approximation. As the excitation photons are directly coupled to the C exciton transition of *m*LW constituents, the EPC strength of a vdWH LB phonon can be approximated by the sum of the weighting factors of its normal mode displacements from all the LB modes in the corresponding *m*LW flake, in which the weighting factors are given by the projection between its wave function components (ψ, i.e., normal mode displacements) among the *m*LW constituent and those (φ_j) of the $LB_{m,m-j}$ ($j = 1, 2, \ldots, m-1$) modes in the *m*LW flake, that is, $p_j = |\langle \varphi_j | \psi \rangle|$. As a consequence, the Raman intensity of LB modes in vdWHs is proportional to $p^2 = \sum_{j}\rho_{j}p^{2}_{j}$, with ρ_j representing the Raman intensity of $LB_{m,\,m-j}$ mode in the *m*LW flake. The calculated relative intensity of the LB modes in 39L-hBN/3LW is shown in Fig. 12.9E, which is in good agreement with the experimental results. On the other hand, based on the interlayer bond polarizability, the Raman intensity is related to the square of the change of a system's polarizability ($\Delta\alpha^2$) [75], which is associated with the interlayer bond polarizability and bond vector, that is, $\Delta\alpha = \sum_i \alpha'_i \cdot \Delta z_i$, with α'_i and z_i representing the polarizability derivative of the entire layer *i* with respective to the vibrations parallel to the normal (*z*) and the normal displacements of layer *i* for one LB mode calculated by Eq. (12.6), respectively. Notably, for the LB modes, only the polarizability derivatives of the top and bottom layers in hBN and WS_2 constituents should be taken into account, as shown in Fig. 12.9E, which can be represented with the fitted parameters η(BN), η(W), and η(I). η(BN), η(W), and η(I) are related to the interlayer bond properties in hBN, WS_2 constituents, and that at the interface, respectively. The relative Raman intensity of LB modes in 39L-hBN/3LW can be well reproduced by η(I)/η(W) = 0.3 and η(BN)/η(W) = 0.001. The corresponding calculated Raman intensities are depicted in Fig. 12.9F [55]. Similar analyses are also applicable to the Raman spectroscopy and EPC of LB modes in other vdWHs, shedding light on manipulating the EPC of interlayer phonons in vdWHs by engineering the interface and varying the vdWH assemblies.

12.6 Second-harmonic generation

SHG is a nonlinear optical effect, where two photons with the same frequency interact with a nonlinear material to generate a new photon with twice the energy of the incident photons. The SHG intensity depends on the second-order nonlinear susceptibility ($\chi^{(2)}$) of the nonlinear material, which is zero for a material with inversion symmetry within the electric dipole approximation, similar to other even-order nonlinear optical phenomena [77, 78]. The electric-dipole-allowed SHG is known to be time invariant, denoted as i-type. The $\chi^{(2)}$ tensor related to the i-type SHG provides the signature of the crystallographic symmetry of a crystal and determines the SHG intensity, suggesting a method to identify the lattice structure and symmetry. To obtain a strong SHG, the intense pulsed laser is commonly utilized to perform the SHG measurement with careful alignment for phase matching.

As known, the ONL MX_2 does not possess an inversion center, while the ENL and bulk MX_2 exhibit inversion symmetry. Fig. 12.10A and B represents the optical image of 1–3L MoS_2 and the corresponding SHG mapping, respectively [79]. The 1LM and trilayer MoS_2 (3LM) exhibit strong SHG intensity, while the SHG is absent in 2LM, consistent with the prediction of i-type SHG. In addition, the weaker SHG intensity in 3LM than that of 1LM can be understood by the wave propagation effects [80]. As the sign of $\chi^{(2)}$ for adjacent layers alternates, the signals from adjacent layers in ONL ($N > 1$) MoS_2 would cancel each other, leading to a weaker SHG intensity than that of 1LM. On the other hand, the band gap of a material relative to the SHG energy would influence the SHG intensity. For example, the common photon energy of SHG (e.g., 3.1 eV) is higher than the bandgap of MoS_2 (~1.90 eV); thus, the SHG signal would be absorbed by MoS_2. The increased absorption of MoS_2 with increasing N will result in decreased SHG intensity. On the contrary, due to the large bandgap of hBN, the SHG photons cannot be absorbed, leading to increasing SHG intensity with respect to N [80].

The SHG intensity is also sensitive to the crystal symmetry and crystallographic orientation. As a result, the polarization-resolved SHG intensity can be utilized to distinguish the crystallographic structure and orientation [79, 80]. The generated SHG intensity of ONL MoS_2 in parallel ($I_{\parallel}$) and perpendicular ($I_{\perp}$) configurations as a function of the angle (ϕ) between the excitation polarization and the crystallographic orientation (x-direction, i.e., armchair direction shown in Fig. 12.10C) can be represented by

$$I_{\parallel} = I_0 \cos^2(3(\phi + \phi_0)), \tag{12.7}$$

$$I_{\perp} = I_0 \sin^2(3(\phi + \phi_0)), \tag{12.8}$$

respectively, where ϕ_0 is the initial crystallographic orientation of the MoS_2 sample. By fitting the experimental data with Eq. (12.7) or (12.8), ϕ_0 can be obtained. In addition to the SHG in MX_2, the N-dependent and strong SHG is recently found to be modulated by the stacking orders in various 2DMs, such as anisotropic ReS_2 [81], GaSe polytypes [82], etc.

Intriguingly, the layered antiferromagnetic order in material with inversion symmetric lattice can also raise the presence of SHG signals, which can be ascribed to the breakdown of the spatial-inversion symmetry and time-reversal symmetry, denoted as c-type [76, 83, 84]. The recent emergence of 2D magnets [2, 16, 17, 85] provides an ideal platform for investigating the c-type SHG effects. As known, the few-layer CrI_3 exhibits antiferromagnetic interlayer coupling and ferromagnetic coupling within a rigid layer [2, 86]. Fig. 12.10D shows the 1L CrI_3 with centrosymmetric

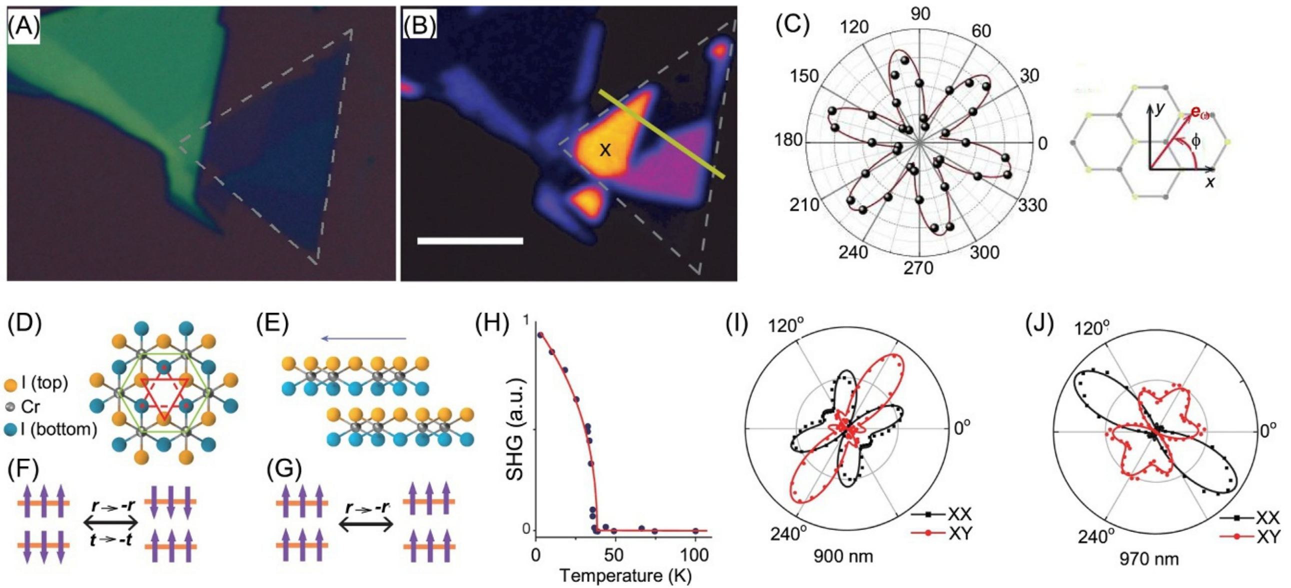

Fig. 12.10 (A) Optical image of 1–3L MoS_2. (B) SHG from the MoS_2 flake shown in (A) excited at 1.55 eV. Stronger SHG intensity is represented by *brighter color*. The scale bar is 5 μm. (C) Polar plot of SHG intensity from 1LM with varying angle between the incident light polarization and the *x*-direction shown in the right panel. (D) Atomic structure of 1L CrI_3, with a hexagon (*green*) formed by six Cr atoms (*gray*) and two equilateral triangles (*solid and dashed red lines*) formed by I atoms of the top (*orange*) and bottom layers. (E) The side view of 2L CrI_3 with a lateral translation. (F) Schematic diagram of interlayer antiferromagnetic states of 2L CrI_3, where spatial-inversion ($\boldsymbol{r} \rightarrow -\boldsymbol{r}$) and time-inversion ($t \rightarrow -t$) operations can change one state to the other. (G) Schematic diagram of interlayer ferromagnetic states of 2L CrI_3 showing a centrosymmetric spin-lattice structure. (H) SHG intensity of 2L CrI_3 with varying temperature (T). The *red solid line* is following the power law [76] $|1-(T/T_c)^{2\beta}|$ for $T < T_c$, in which T_c is the critical temperature and β is the critical exponent. Polarization-resolved SHG intensity at 0 T excited at (I) 900 and (J) 970 nm. The excitation and detection are linearly polarized, with XX and XY indicating co- and cross-linearly polarization light, respectively.
(A–C) Adapted from L.M. Malard, T.V. Alencar, A.P.M. Barboza, K.F. Mak, A.M. de Paula, Observation of intense second harmonic generation from MoS_2 atomic crystals, Phys. Rev. B 87 (20) (2013) 201401, https://doi.org/10.1103/PhysRevB.87.201401; (D–J) adapted from Z. Sun, Y. Yi, T. Song, G. Clark, B. Huang, Y. Shan, S. Wu, D. Huang, C. Gao, Z. Chen, M. McGuire, T. Cao, D. Xiao, W.-T. Liu, W. Yao, X. Xu, S. Wu, Giant nonreciprocal second-harmonic generation from antiferromagnetic bilayer CrI_3, Nature 572 (7770) (2019) 497–501, https://doi.org/10.1038/s41586-019-1445-3.

lattice structure. By stacking two monolayers together (Fig. 12.10E), the lattice structure of 2L CrI_3 also exhibits centrosymmetry, regardless of any rigid translation between two monolayers. Within the electric dipole approximation, the SHG signal is prohibited in 2L CrI_3. However, below the critical temperature (T_c), the two monolayers of 2L CrI_3 would show antiferromagnetic interlayer coupling, as shown in Fig. 12.10F, that is, all spins in a rigid layer pointing outwards or inwards but different directions in its adjacent layer, which would break both spatial-inversion and time-reversal symmetries. Thus, it is expected to observe the c-type SHG signal in 2L CrI_3 below T_c. When applying an out-of-plane magnetic field to 2L CrI_3, it becomes ferromagnetic and the inversion symmetry restores, as demonstrated in Fig. 12.10G. The measured SHG intensity of 2L CrI_3 as a function of temperature (T) at zero magnetic field is depicted in Fig. 12.10H. The strong dependence of SHG on T is in line with the above prediction. The SHG is absent above T_c, further confirming the inversion symmetry of 2L CrI_3 [83]. In addition, the linear polarization-resolved SHG was utilized to provide information about the lattice symmetry and initial crystallographic orientation. As shown in Fig. 12.10I, the polarization dependence of 2L CrI_3 under 900 nm excitation at 0 T shows six asymmetric lobes under both co- and cross-linear polarization configurations, suggesting the broken threefold rotational symmetry in 2L CrI_3. The polarization-dependent patterns can be fitted by the c-type $\chi^{(2)}$ tensor related to C_{2h} symmetry, which implies the monoclinic stacking configuration for 2L CrI_3 [83]. The polarization-resolved SHG signal under 970 nm excitation also displaces an in-plane C_2 axis about 145 degrees with respective to the horizontal direction (Fig. 12.10J), similar to that under 900 nm excitation though details of SHG patterns vary. This further confirms the monoclinic stacking for 2L CrI_3. All these works related to SHG indicate that it is a highly sensitive probe of subtle lattice symmetry and magnetic order, opening up possibilities for the characterizations and applications of 2DMs in nonlinear optical devices.

12.7 Conclusion

In this chapter, we have addressed the recent optical spectroscopy study of 2DMs. The discussion begins with an overview of a broad portfolio of emergent 2DMs and related vdWHs, which exhibit various extraordinary physical properties modified by number of layers, stacking order, defect engineering, and even assemblies in vdWHs. The OC and differential reflection spectrum in 2DMs and vdWHs have emerged as powerful tools to identify the thickness and peak positions of excitons. We have demonstrated the strong excitonic effects and valley polarization in MX_2 via PL spectroscopy. The experimental evidence for the moiré excitons in vdWHs consisting of constituents with nearly same lattice constants is also elucidated using PL spectroscopy. Following that we give a detailed introduction of the optical spectroscopy study based on light scattering, including Rayleigh scattering and Raman scattering. Rayleigh scattering shows strong thickness dependence. Besides, Raman spectroscopy is reviewed by taking pristine 2DMs, twisted 2DMs, and vdWHs as examples, which reveal the lattice structure and symmetry, interlayer coupling, thickness-dependent Davydov splitting, electronic band structure, and EPC in the corresponding 2D systems. The optical spectroscopy related to nonlinear optical effects, that is, SHG, is also elucidated, unveiling the applications of electric dipole allowed SHG and time-noninvariant/nonreciprocal SHG in distinguishing the lattice symmetry and magnetic orders, respectively. The sensitivity of optical spectroscopy to the electronic band structure, lattice structure and symmetry, defects, doping, number of layers, and stacking order of 2DMs indicates it as a powerful tool for related physical phenomena that are otherwise challenging to probe, and also being important for the characterizations and applications of optoelectronic devices based on 2DMs.

Acknowledgments

We acknowledge support from the National Natural Science Foundation of China (Grant Nos. 12004377 and 11874350), and the CAS Key Research Program of Frontier Sciences (Grant Nos. ZDBS-LY-SLH004 and XDPB22).

References

[1] N. Mounet, M. Gibertini, P. Schwaller, D. Campi, A. Merkys, A. Marrazzo, T. Sohier, I.E. Castelli, A. Cepellotti, G. Pizzi, N. Marzari, Two-dimensional materials from high-throughput computational exfoliation of experimentally known compounds, Nat. Nanotechnol. 13 (3) (2018) 246–252, https://doi.org/10.1038/s41565-017-0035-5.

[2] B. Huang, G. Clark, E. Navarro-Moratalla, R. Klein, R.D. Cheng, K.L. Seyler, D. Zhong, E. Schmidgall, M.A. McGuire, W. Yao, D. Xiao, P. Jarillo-Herrero, X. Xu, Layer-dependent ferromagnetism in a van der Waals crystal down to the monolayer limit, Nature 546 (7657) (2017) 270–273, https://doi.org/10.1038/nature22391.

[3] P.-H. Tan, Raman Spectroscopy of Two-Dimensional Materials, Springer Nature Singapore Pte Ltd., Singapore, 2019, https://doi.org/10.1007/978-981-13-1828-3.

[4] K.S. Novoselov, A.K. Geim, S.V. Morozov, D. Jiang, Y. Zhang, S.V. Dubonos, I.V. Grigorieva, A.A. Firsov, Electric field effect in atomically thin carbon films, Science 306 (5696) (2004) 666–669, https://doi.org/10.1126/science.1102896.

[5] J.-B. Wu, M.-L. Lin, X. Cong, H.-N. Liu, P.-H. Tan, Raman spectroscopy of graphene-based materials and its applications in related devices, Chem. Soc. Rev. 47 (5) (2018) 1822–1873, https://doi.org/10.1039/c6cs00915h.

[6] G. Cassabois, P. Valvin, B. Gil, Hexagonal boron nitride is an indirect bandgap semiconductor, Nat. Photon. 10 (2016) 262–266, https://doi.org/10.1038/nphoton.2015.277.

[7] X. Zhang, X.-F. Qiao, W. Shi, J.-B. Wu, D.-S. Jiang, P.-H. Tan, Phonon and Raman scattering of two-dimensional transition metal dichalcogenides from monolayer, multilayer to bulk material, Chem. Soc. Rev. 44 (9) (2015) 2757–2785, https://doi.org/10.1039/C4CS00282B.

[8] M. Osada, T. Sasaki, Two-dimensional dielectric nanosheets: novel nanoelectronics from nanocrystal building blocks, Adv. Mater. 24 (2) (2012) 210–228, https://doi.org/10.1002/adma.201103241.

[9] E. Shi, Y. Gao, B.P. Finkenauer, Akriti, A.H. Coffey, L. Dou, Two-dimensional halide perovskite nanomaterials and heterostructures, Chem. Soc. Rev. 47 (16) (2018) 6046–6072, https://doi.org/10.1039/C7CS00886D.

[10] X. Xi, Z. Wang, W. Zhao, J.-H. Park, K.T. Law, H. Berger, L. Forró, J. Shan, K.F. Mak, Ising pairing in superconducting $NbSe_2$ atomic layers, Nat. Phys. 12 (2) (2016) 139–143,- https://doi.org/10.1038/nphys3538.

[11] B. Sipos, A.F. Kusmartseva, A. Akrap, H. Berger, L. Forró, E. Tutiš, From Mott state to superconductivity in 1T-TaS_2, Nat. Mater. 7 (12) (2008) 960–965, https://doi.org/10.1038/nmat2318.

[12] M.N. Ali, J. Xiong, S. Flynn, J. Tao, Q.D. Gibson, L.M. Schoop, T. Liang, N. Haldolaarachchige, M. Hirschberger, N.P. Ong, R.J. Cava, Large, non-saturating magnetoresistance in WTe_2, Nature 514 (7521) (2014) 205–208, https://doi.org/10.1038/nature13763.

[13] K.F. Mak, C. Lee, J. Hone, J. Shan, T.F. Heinz, Atomically thin MoS_2: a new direct-gap semiconductor, Phys. Rev. Lett. 105 (13) (2010) 136805, https://doi.org/10.1103/PhysRevLett.105.136805.

[14] Q.H. Wang, K. Kalantar-Zadeh, A. Kis, J.N. Coleman, M.S. Strano, Electronics and optoelectronics of two-dimensional transition metal dichalcogenides, Nat. Nanotechnol. 7 (11) (2012) 699–712, https://doi.org/10.1038/nnano.2012.193.

[15] C.N. Eads, D. Bandak, M.R. Neupane, D. Nordlund, O.L.A. Monti, Anisotropic attosecond charge carrier dynamics and layer decoupling in quasi-2D layered SnS_2, Nat. Commun. 8 (2017) 1369, https://doi.org/10.1038/s41467-017-01522-3.

[16] J.-U. Lee, S. Lee, J.H. Ryoo, S. Kang, T.Y. Kim, P. Kim, C.-H. Park, J.-G. Park, H. Cheong, Ising-type magnetic ordering in atomically thin $FePS_3$, Nano Lett. 16 (12) (2016) 7433–7438, https://doi.org/10.1021/acs.nanolett.6b03052.

[17] K. Kim, S.Y. Lim, J.-U. Lee, S. Lee, T.Y. Kim, K. Park, G.S. Jeon, C.-H. Park, J.-G. Park, H. Cheong, Suppression of magnetic ordering in XXZ-type antiferromagnetic monolayer $NiPS_3$, Nat. Commun. 10 (1) (2019) 345, https://doi.org/10.1038/s41467-018-08284-6.

[18] L. Liang, J. Zhang, B.G. Sumpter, Q.-H. Tan, P.-H. Tan, V. Meunier, Low-frequency shear and layer-breathing modes in Raman scattering of two-dimensional materials, ACS Nano 11 (12) (2017) 11777–11802, https://doi.org/10.1021/acsnano.7b06551.

[19] S.N. Shirodkar, U.V. Waghmare, Emergence of ferroelectricity at a metal-semiconductor transition in a 1T monolayer of MoS_2, Phys. Rev. Lett. 112 (15) (2014) 157601, https://doi.org/10.1103/PhysRevLett.112.157601.

[20] J.-B. Wu, X. Zhang, M. Ijäs, W.-P. Han, X.-F. Qiao, X.-L. Li, D.-S. Jiang, A.C. Ferrari, P.-H. Tan, Resonant Raman spectroscopy of twisted multilayer graphene, Nat. Commun. 5 (2014) 5309.

[21] K. Liu, L. Zhang, T. Cao, C. Jin, D. Qiu, Q. Zhou, A. Zettl, P. Yang, S.G. Louie, F. Wang, Evolution of interlayer coupling in twisted molybdenum disulfide bilayers, Nat. Commun. 5 (2014) 4966, https://doi.org/10.1038/ncomms5966.

[22] K.S. Novoselov, A.H.C. Neto, Two-dimensional crystals-based heterostructures: materials with tailored properties, Phys. Scr. 2012 (146) (2012) 014006, https://doi.org/10.1088/0031-8949/2012/T146/014006.

[23] R. Bistritzer, A.H. MacDonald, Moiré bands in twisted double-layer graphene, Proc. Natl Acad. Sci. USA 108 (30) (2011) 12233–12237, https://doi.org/10.1073/pnas.1108174108.

[24] H. Yu, G.-B. Liu, J. Tang, X. Xu, W. Yao, Moiré excitons: from programmable quantum emitter arrays to spin-orbit-coupled artificial lattices, Sci. Adv. 3 (11) (2017) e1701696, https://doi.org/10.1126/sciadv.1701696.

[25] M.-L. Lin, Q.-H. Tan, J.-B. Wu, X.-S. Chen, J.-H. Wang, Y.-H. Pan, X. Zhang, X. Cong, J. Zhang, W. Ji, P.-A. Hu, K.-H. Liu, P.-H. Tan, Moiré phonons in twisted bilayer MoS_2, ACS Nano 12 (8) (2018) 8770–8780, https://doi.org/10.1021/acsnano.8b05006.

[26] Y. Cao, V. Fatemi, A. Demir, S. Fang, S.L. Tomarken, J.Y. Luo, J.D. Sanchez-Yamagishi, K. Watanabe, T. Taniguchi, E. Kaxiras, R.C. Ashoori, P. Jarillo-Herrero, Correlated

insulator behaviour at half-filling in magic-angle graphene superlattices, Nature 556 (7699) (2018) 80–84, https://doi.org/10.1038/nature26154.

[27] K.L. Seyler, P. Rivera, H. Yu, N.P. Wilson, E.L. Ray, D.G. Mandrus, J. Yan, W. Yao, X. Xu, Signatures of moiré-trapped valley excitons in $MoSe_2/WSe_2$ heterobilayers, Nature 567 (7746) (2019) 66–70, https://doi.org/10.1038/s41586-019-0957-1.

[28] K. Tran, G. Moody, F. Wu, X. Lu, J. Choi, K. Kim, A. Rai, D.A. Sanchez, J. Quan, A. Singh, J. Embley, A. Zepeda, M. Campbell, T. Autry, T. Taniguchi, K. Watanabe, N. Lu, S.K. Banerjee, K.L. Silverman, S. Kim, E. Tutuc, L. Yang, A.H. MacDonald, X. Li, Evidence for moiré excitons in van der Waals heterostructures, Nature 567 (7746) (2019) 71–75, https://doi.org/10.1038/s41586-019-0975-z.

[29] C. Jin, E.C. Regan, A. Yan, M. Iqbal Bakti Utama, D. Wang, S. Zhao, Y. Qin, S. Yang, Z. Zheng, S. Shi, K. Watanabe, T. Taniguchi, S. Tongay, A. Zettl, F. Wang, Observation of moiré excitons in WSe_2/WS_2 heterostructure superlattices, Nature 567 (7746) (2019) 76–80, https://doi.org/10.1038/s41586-019-0976-y.

[30] Z.H. Ni, H.M. Wang, J. Kasim, H.M. Fan, T. Yu, Y.H. Wu, Y.P. Feng, Z.X. Shen, Graphene thickness determination using reflection and contrast spectroscopy, Nano Lett. 7 (9) (2007) 2758–2763, https://doi.org/10.1021/nl071254m.

[31] X.-L. Li, W.-P. Han, J.-B. Wu, X.-F. Qiao, J. Zhang, P.-H. Tan, Layer-number dependent optical properties of 2D materials and their application for thickness determination, Adv. Funct. Mater. 27 (2017) 1604468, https://doi.org/10.1002/adfm.201604468.

[32] Y. Lu, X.-L. Li, X. Zhang, J.-B. Wu, P.-H. Tan, Optical contrast determination of the thickness of SiO_2 film on Si substrate partially covered by two-dimensional crystal flakes, Sci. Bull. 60 (8) (2015) 806–811, https://doi.org/10.1007/s11434-015-0774-3.

[33] X.-L. Li, X.-F. Qiao, W.-P. Han, Y. Lu, Q.-H. Tan, X.-L. Liu, P.-H. Tan, Layer number identification of intrinsic and defective multilayered graphenes up to 100 layers by the Raman mode intensity from substrates, Nanoscale 7 (17) (2015) 8135–8141, https://doi.org/10.1039/c5nr01514f.

[34] W. Zhao, Z. Ghorannevis, L. Chu, M. Toh, C. Kloc, P.-H. Tan, G. Eda, Evolution of electronic structure in atomically thin sheets of WS_2 and WSe_2, ACS Nano 7 (1) (2013) 791–797, https://doi.org/10.1021/nn305275h.

[35] C. Ruppert, O.B. Aslan, T.F. Heinz, Optical properties and band gap of single- and few-layer $MoTe_2$ crystals, Nano Lett. 14 (11) (2014) 6231–6236, https://doi.org/10.1021/nl502557g.

[36] D.Y. Qiu, F.H. da Jornada, S.G. Louie, Optical spectrum of MoS_2: many-body effects and diversity of exciton states, Phys. Rev. Lett. 111 (21) (2013) 216805, https://doi.org/10.1103/PhysRevLett.111.216805.

[37] N. Mizuochi, T. Makino, H. Kato, D. Takeuchi, M. Ogura, H. Okushi, M. Nothaft, P. Neumann, A. Gali, F. Jelezko, J. Wrachtrup, S. Yamasaki, Electrically driven single-photon source at room temperature in diamond, Nat. Photon. 6 (5) (2012) 299–303,- https://doi.org/10.1038/nphoton.2012.75.

[38] W. Xu, W. Liu, J.F. Schmidt, W. Zhao, X. Lu, T. Raab, C. Diederichs, W. Gao, D.V. Seletskiy, Q. Xiong, Correlated fluorescence blinking in two-dimensional semiconductor heterostructures, Nature 541 (2017) 62–67, https://doi.org/10.1038/nature20601.

[39] K.F. Mak, K. He, J. Shan, T.F. Heinz, Control of valley polarization in monolayer MoS_2 by optical helicity, Nat. Nanotechnol. 7 (8) (2012) 494–498, https://doi.org/10.1038/nnano.2012.96.

[40] T. Cao, G. Wang, W.P. Han, H.Q. Ye, C.R. Zhu, J.R. Shi, Q. Niu, P.H. Tan, E. Wang, B.L. Liu, J. Feng, Valley-selective circular dichroism of monolayer molybdenum disulphide, Nat. Commun. 3 (2012) 887, https://doi.org/10.1038/ncomms1882.

[41] H. Zeng, J. Dai, W. Yao, D. Xiao, X. Cui, Valley polarization in MoS_2 monolayers by optical pumping, Nat. Nanotechnol. 7 (8) (2012) 490–493, https://doi.org/10.1038/nnano.2012.95.

[42] K. He, N. Kumar, L. Zhao, Z. Wang, K.F. Mak, H. Zhao, J. Shan, Tightly bound excitons in monolayer WSe_2, Phys. Rev. Lett. 113 (2) (2014) 026803, https://doi.org/10.1103/PhysRevLett.113.026803.

[43] Z. Ye, T. Cao, K. O'Brien, H. Zhu, X. Yin, Y. Wang, S.G. Louie, X. Zhang, Probing excitonic dark states in single-layer tungsten disulphide, Nature 513 (7517) (2014) 214–218,- https://doi.org/10.1038/nature13734.

[44] D. Xiao, G.-B. Liu, W. Feng, X. Xu, W. Yao, Coupled spin and valley physics in monolayers of MoS_2 and Other group-VI dichalcogenides, Phys. Rev. Lett. 108 (19) (2012) 196802, https://doi.org/10.1103/PhysRevLett.108.196802.

[45] K.F. Mak, K. He, C. Lee, G.H. Lee, J. Hone, T.F. Heinz, J. Shan, Tightly bound trions in monolayer MoS_2, Phys. Rev. Lett. 12 (3) (2013) 207–211, https://doi.org/10.1038/nmat3505.

[46] Y.-M. He, G. Clark, J.R. Schaibley, Y. He, M.-C. Chen, Y.-J. Wei, X. Ding, Q. Zhang, W. Yao, X. Xu, C.-Y. Lu, J.-W. Pan, Single quantum emitters in monolayer semiconductors, Nat. Nanotechnol. 10 (6) (2015) 497–502, https://doi.org/10.1038/nnano.2015.75.

[47] C. Chakraborty, L. Kinnischtzke, K.M. Goodfellow, R. Beams, A.N. Vamivakas, Voltage-controlled quantum light from an atomically thin semiconductor, Nat. Nanotechnol. 10 (6) (2015) 507–511, https://doi.org/10.1038/nnano.2015.79.

[48] A. Srivastava, M. Sidler, A.V. Allain, D.S. Lembke, A. Kis, A. Imamoğlu, Optically active quantum dots in monolayer WSe_2, Nat. Nanotechnol. 10 (6) (2015) 491–496, https://doi.org/10.1038/nnano.2015.60.

[49] A. Jorio, R. Saito, G. Dresselhaus, M.S. Dresselhaus, Raman Spectroscopy in Graphene Related Systems, Wiley-VCH Verlag GmbH & Co. KGaA, Weinheim, 2011.

[50] C. Casiraghi, A. Hartschuh, E. Lidorikis, H. Qian, H. Harutyunyan, T. Gokus, K.S. Novoselov, A.C. Ferrari, Rayleigh imaging of graphene and graphene layers, Nano Lett. 7 (9) (2007) 2711–2717, https://doi.org/10.1021/nl071168m.

[51] J.-B. Wu, H. Wang, X.-L. Li, H. Peng, P.-H. Tan, Raman spectroscopic characterization of stacking configuration and interlayer coupling of twisted multilayer graphene grown by chemical vapor deposition, Carbon 110 (2016) 225–231, https://doi.org/10.1016/j.carbon.2016.09.006.

[52] L.M. Malard, M.A. Pimenta, G. Dresselhaus, M.S. Dresselhaus, Raman spectroscopy in graphene, Phys. Rep. 473 (5) (2009) 51–87, https://doi.org/10.1016/j.physrep.2009.02.003.

[53] A.C. Ferrari, D.M. Basko, Raman spectroscopy as a versatile tool for studying the properties of graphene, Nat. Nanotechnol. 8 (4) (2013) 235–246, https://doi.org/10.1038/nnano.2013.46.

[54] Q.J. Song, Q.H. Tan, X. Zhang, J.B. Wu, B.W. Sheng, Y. Wan, X.Q. Wang, L. Dai, P.H. Tan, Physical origin of Davydov splitting and resonant Raman spectroscopy of Davydov components in multilayer $MoTe_2$, Phys. Rev. B 93 (11) (2016) 115409, https://doi.org/10.1103/PhysRevB.93.115409.

[55] M.-L. Lin, Y. Zhou, J.-B. Wu, X. Cong, X.-L. Liu, J. Zhang, H. Li, W. Yao, P.-H. Tan, Cross-dimensional electron-phonon coupling in van der Waals heterostructures, Nat. Commun. 10 (2019) 2419, https://doi.org/10.1038/s41467-019-10400-z.

[56] P.H. Tan, W.P. Han, W.J. Zhao, Z.H. Wu, K. Chang, H. Wang, Y.F. Wang, N. Bonini, N. Marzari, N. Pugno, G. Savini, A. Lombardo, A.C. Ferrari, The shear mode of multilayer graphene, Nat. Mater. 11 (2012) 294–300, https://doi.org/10.1038/NMAT3245.

[57] J.-B. Wu, Z.-X. Hu, X. Zhang, W.-P. Han, Y. Lu, W. Shi, X.-F. Qiao, M. Ijiäs, S. Milana, W. Ji, A.C. Ferrari, P.-H. Tan, Interface coupling in twisted multilayer graphene by resonant Raman spectroscopy of layer breathing modes, ACS Nano 9 (7) (2015) 7440–7449.

[58] X. Zhang, Q.-H. Tan, J.-B. Wu, W. Shi, P.-H. Tan, Review on the Raman spectroscopy of different types of layered materials, Nanoscale 8 (12) (2016) 6435–6450, https://doi.org/10.1039/c5nr07205k.

[59] X.-F. Qiao, J.-B. Wu, L. Zhou, J. Qiao, W. Shi, T. Chen, X. Zhang, J. Zhang, W. Ji, P.-H. Tan, Polytypism and unexpected strong interlayer coupling in two-dimensional layered ReS_2, Nanoscale 8 (15) (2016) 8324–8332, https://doi.org/10.1039/C6NR01569G.

[60] K. Kim, J.-U. Lee, D. Nam, H. Cheong, Davydov splitting and excitonic resonance effects in Raman spectra of few-layer $MoSe_2$, ACS Nano 10 (8) (2016) 8113–8120, https://doi.org/10.1021/acsnano.6b04471.

[61] Q.-H. Tan, Y.-J. Sun, X.-L. Liu, Y. Zhao, Q. Xiong, P.-H. Tan, J. Zhang, Observation of forbidden phonons, Fano resonance and dark excitons by resonance Raman scattering in few-layer WS_2, 2D Mater. 4 (3) (2017) 031007, https://doi.org/10.1088/2053-1583/aa79bb.

[62] Q.-H. Tan, X. Zhang, X.-D. Luo, J. Zhang, P.-H. Tan, Layer-number dependent high-frequency vibration modes in few-layer transition metal dichalcogenides induced by interlayer couplings, J. Semicond. 38 (3) (2017) 031006, https://doi.org/10.1088/1674-4926/38/3/031006.

[63] C. Cong, T. Yu, Enhanced ultra-low-frequency interlayer shear modes in folded graphene layers, Nat. Commun. 5 (2014) 4709, https://doi.org/10.1038/ncomms5709.

[64] S. Huang, X. Ling, L. Liang, J. Kong, H. Terrones, V. Meunier, M.S. Dresselhaus, Probing the interlayer coupling of twisted bilayer MoS_2 using photoluminescence spectroscopy, Nano Lett. 14 (10) (2014) 5500–5508, https://doi.org/10.1021/nl5014597.

[65] A.A. Puretzky, L. Liang, X. Li, K. Xiao, B.G. Sumpter, V. Meunier, D.B. Geohegan, Twisted $MoSe_2$ bilayers with variable local stacking and interlayer coupling revealed by low-frequency Raman spectroscopy, ACS Nano 10 (2) (2016) 2736–2744, https://doi.org/10.1021/acsnano.5b07807.

[66] V. Carozo, C.M. Almeida, E.H. Ferreira, L.G. Cançado, C.A. Achete, A. Jorio, Raman signature of graphene superlattices, Nano Lett. 11 (11) (2011) 4527–4534.

[67] P. Parzefall, J. Holler, M. Scheuck, A. Beer, K.Q. Lin, B. Peng, B. Monserrat, P. Nagler, M. Kempf, T. Korn, C. Schüller, Moiré phonons in twisted $MoSe_2$-WSe_2 heterobilayers and their correlation with interlayer excitons, 2D Mater. 8 (3) (2021), https://doi.org/10.1088/2053-1583/abf98e.

[68] H. Yoo, R. Engelke, S. Carr, S. Fang, K. Zhang, P. Cazeaux, S.H. Sung, R. Hovden, A.W. Tsen, T. Taniguchi, K. Watanabe, G.C. Yi, M. Kim, M. Luskin, E.B. Tadmor, E. Kaxiras, P. Kim, Atomic and electronic reconstruction at the van der Waals interface in twisted bilayer graphene, Nat. Mater. 18 (5) (2019) 448–453, https://doi.org/10.1038/s41563-019-0346-z.

[69] A. Weston, Y. Zou, V. Enaldiev, A. Summerfield, N. Clark, V. Zólyomi, A. Graham, C. Yelgel, S. Magorrian, M. Zhou, J. Zultak, D. Hopkinson, A. Barinov, T.H. Bointon, A. Kretinin, N.R. Wilson, P.H. Beton, V.I. Fal'ko, S.J. Haigh, R. Gorbachev, Atomic reconstruction in twisted bilayers of transition metal dichalcogenides, Nat. Nanotechnol. 15 (7) (2020) 592–597, https://doi.org/10.1038/s41565-020-0682-9.

[70] T.I. Andersen, G. Scuri, A. Sushko, K. De Greve, J. Sung, Y. Zhou, D.S. Wild, R.J. Gelly, H. Heo, D. Bérubé, A.Y. Joe, L.A. Jauregui, K. Watanabe, T. Taniguchi, P. Kim, H. Park, M.D. Lukin, Excitons in a reconstructed moiré potential in twisted WSe_2/WSe_2 homobilayers, Nat. Mater. 20 (4) (2021) 480–487, https://doi.org/10.1038/s41563-020-00873-5.

[71] J. Quan, L. Linhart, M.L. Lin, D. Lee, J. Zhu, C.Y. Wang, W.T. Hsu, J. Choi, J. Embley, C. Young, T. Taniguchi, K. Watanabe, C.K. Shih, K. Lai, A.H. MacDonald, P.H. Tan, F. Libisch, X. Li, Phonon renormalization in reconstructed MoS_2 moiré superlattices, Nat. Mater. 20 (2021) 1100–1105, https://doi.org/10.1038/s41563-021-00960-1.

[72] A.C. Gadelha, D.A.A. Ohlberg, C. Rabelo, E.G. Neto, T.L. Vasconcelos, J.L. Campos, J.S. Lemos, V. Ornelas, D. Miranda, R. Nadas, F.C. Santana, K. Watanabe, T. Taniguchi, B. van Troeye, M. Lamparski, V. Meunier, V.H. Nguyen, D. Paszko, J.C. Charlier, L.

C. Campos, L.G. Cançado, G. Medeiros-Ribeiro, A. Jorio, Localization of lattice dynamics in low-angle twisted bilayer graphene, Nature 590 (7846) (2021) 405–409, https://doi.org/10.1038/s41586-021-03252-5.

[73] Y.-C. Leng, M.-L. Lin, Y. Zhou, J.-B. Wu, D. Meng, X. Cong, H. Li, P.-H. Tan, Intrinsic effect of interfacial coupling on the high- frequency intralayer modes in twisted multilayer $MoTe_2$, Nanoscale 13 (21) (2021) 9372–9739, https://doi.org/10.1039/D1NR01309B.

[74] H. Li, J.-B. Wu, F. Ran, M.-L. Lin, X.-L. Liu, Y. Zhao, X. Lu, Q. Xiong, J. Zhang, W. Huang, H. Zhang, P.-H. Tan, Interfacial interactions in van der Waals heterostructures of MoS_2 and graphene, ACS Nano 11 (11) (2017) 11714–11723, https://doi.org/10.1021/acsnano.7b07015.

[75] L. Liang, A.A. Puretzky, B.G. Sumpter, V. Meunier, Interlayer bond polarizability model for stacking-dependent low-frequency Raman scattering in layered materials, Nanoscale 9 (40) (2017) 15340–15355, https://doi.org/10.1039/C7NR05839J.

[76] M. Fiebig, V.V. Pavlov, R.V. Pisarev, Second-harmonic generation as a tool for studying electronic and magnetic structures of crystals: review, J. Opt. Soc. Am. B 22 (1) (2005) 96–118, https://doi.org/10.1364/JOSAB.22.000096.

[77] R.W. Boyd (Ed.), The Nonlinear Optical Susceptibility, Nonlinear Optics, in: third ed., Academic Press, Burlington, 2008, pp. 1–67, https://doi.org/10.1016/B978-0-12-369470-6.00001-0. Chapter 1.

[78] T. Jiang, H. Liu, D. Huang, S. Zhang, Y. Li, X. Gong, Y.-R. Shen, W.-T. Liu, S. Wu, Rayleigh imaging of graphene and graphene layers, Nat. Nanotechnol. 9 (10) (2014) 825–829, https://doi.org/10.1038/nnano.2014.176.

[79] L.M. Malard, T.V. Alencar, A.P.M. Barboza, K.F. Mak, A.M. de Paula, Observation of intense second harmonic generation from MoS_2 atomic crystals, Phys. Rev. B 87 (20) (2013) 201401, https://doi.org/10.1103/PhysRevB.87.201401.

[80] Y. Li, Y. Rao, K.F. Mak, Y. You, S. Wang, C.R. Dean, T.F. Heinz, Probing symmetry properties of few-layer MoS_2 and h-BN by optical second-harmonic generation, Nano Lett. 13 (7) (2013) 3329–3333, https://doi.org/10.1021/nl401561r.

[81] Y. Song, S. Hu, M.-L. Lin, X. Gan, P.-H. Tan, J. Zhao, Extraordinary second harmonic generation in ReS_2 atomic crystals, ACS Photonics 5 (9) (2018) 3485–3491, https://doi.org/10.1021/acsphotonics.8b00685.

[82] W. Jie, X. Chen, D. Li, L. Xie, Y.Y. Hui, S.P. Lau, X. Cui, J. Hao, Layer-dependent nonlinear optical properties and stability of non-centrosymmetric modification in few-layer GaSe sheets, Angew. Chem. Int. Ed. 54 (4) (2015) 1185–1189, https://doi.org/10.1002/anie.201409837.

[83] Z. Sun, Y. Yi, T. Song, G. Clark, B. Huang, Y. Shan, S. Wu, D. Huang, C. Gao, Z. Chen, M. McGuire, T. Cao, D. Xiao, W.-T. Liu, W. Yao, X. Xu, S. Wu, Giant nonreciprocal second-harmonic generation from antiferromagnetic bilayer CrI_3, Nature 572 (7770) (2019) 497–501, https://doi.org/10.1038/s41586-019-1445-3.

[84] P. Němec, M. Fiebig, T. Kampfrath, A.V. Kimel, Antiferromagnetic opto-spintronics, Nat. Phys. 14 (3) (2018) 229–241, https://doi.org/10.1038/s41567-018-0051-x.

[85] C. Gong, L. Li, Z. Li, H. Ji, A. Stern, Y. Xia, T. Cao, W. Bao, C. Wang, Y. Wang, Z.Q. Qiu, R.J. Cava, S.G. Louie, J. Xia, X. Zhang, Discovery of intrinsic ferromagnetism in two-dimensional van der Waals crystals, Nature 546 (7657) (2017) 265–269, https://doi.org/10.1038/nature22060.

[86] P. Jiang, C. Wang, D. Chen, Z. Zhong, Z. Yuan, Z.-Y. Lu, W. Ji, Stacking tunable interlayer magnetism in bilayer CrI_3, Phys. Rev. B 99 (14) (2019) 144401, https://doi.org/10.1103/PhysRevB.99.144401.